University of Padova

Department of Information Engineering
Master's degree in Bioengineering

Location of the optic disc in scanning laser ophthalmoscope images and validation

Student:
Sabrina Mattera
Student ID:
1159835

Supervisor:
Prof. Andrea Facchinetti
Co-supervisor:
Prof. Emanuele Trucco

08 July 2019

Academic year 2018/2019

Contents

Abstract

In this thesis we propose two methods for optic disc (OD) detection and segmentation in scanning laser ophthalmoscope (SLO) images of the human retina.
The OD is one of the main landmark for locating other components in the retina, for vessel tracking and retinal zones identification. Moreover, it is well-known that the OD appearance is linked to glaucoma. Hence, an accurate and reliable detection is needed.
Many algorithms have been proposed for OD detection in fundus camera images but hardly any for SLO images. In these images, the OD appears as a dark elliptical shape spot with high contrast between the inner and outer region and poorer contrast with the vessels. For this reason the techniques working with fundus camera images are not suitable for SLO images.
Both methods locate a ROI containing the OD first and then segment the OD. The first method segments the OD via morphological operations. The second method extracts hand-crafted features within the ROI and selects the OD contour points by an optimization in the space of the possible shapes of a deformable contour.
We tested the algorithms with 1536x1536 images from a Heildelberg SPECTRALIS SLO camera. The second algorithm performs better than the first one; it achieves an average accuracy of 90% on a pilot dataset of 50 images annotated by four expert ophthalmologists.
We compared the resulting contours with those obtained by a validated OD algorithm on registered fundus camera images; hence, in our work, we proposed a semi-automatic approach to register these two kind of images, too.
This work was supported by NHS Lothian R&D, and Edinburgh Imaging and the Edinburgh Clinical Research Facility at the University of Edinburgh.
The project has been developed during the ERASMUS Mobility Studentships program at the CVIP department of Dundee University.

Keywords: retinal image analysis, optic disc, validation, image registration.

Acknowledgements

I just wanna to thank everybody who have contributed to this work.
A special thanks to prof. Emanuele Trucco, Manuel, for being an inspiration and for having taught me so much during the months spent in Dundee, to his great ability in teaching and to his passion to do this.
Thanks to my supervisor, prof. Andrea Facchinetti, for his availability, attitude and competence.
Thanks also to the four ophthalmologists, always available and for their kindness and patience in annotating the images.
And to the VAMPIRE group for sharing ideas and knowledge, this incredible and amazing experience with them gave me so much. I will remember them forever. Thanks a lot.
My sincere thanks to Stefano, for having worked together during these months, shared the same experiences and supported each other in times of need.
I would like to thank all the people who love me and have always believed and continue to believe in me. I think I haven't forgotten anyone, but if I've forgotten someone ... Thank you so much for everything.

Chapter 1

Introduction

1.1 About this chapter

Nowadays, in ophthalmology, computer-assisted solutions are employed to help clinicians in diagnosis, screening, as well as in assessing a new treatment. Our contribute is the development of a software for the automatic localization of one of the main landmark in the human retina, the optic disc (OD), in a specific kind of image. In this Chapter we are going to investigate why there is the need of automatic procedures in the study of the human retina and, in particular, for the detection of the OD. We will start from a simple anatomy of the eye, focusing on the retina, and then we will discuss the retinal imaging technologies used in this study.

1.2 Eye structure

The eye is a organ that allows to receive light stimuli from the outside world, that will be converted into visual information by the visual apparatus.

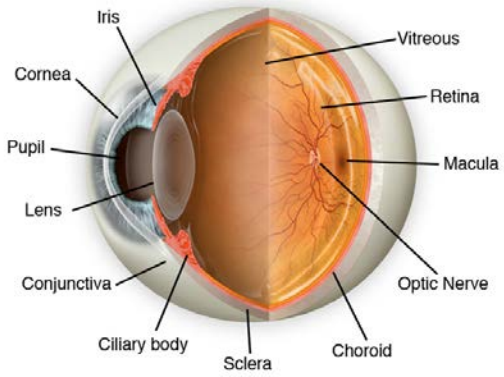

Figure 1.1: Section of human eye.[1]

[1]https://www.brainhq.com/brain-resources/image-gallery/vision-images

Looking into someone's eyes several structures can be recognised[2], Figure 1.1. The **pupil**, a black-looking aperture, allows light to enter the eye; as the size of the pupil changes the more or less light enters. The pupil's size is controlled by a coloured circular muscle surrounding the pupil itself, the **iris**. It is responsible of the eye's colour. Both pupil and iris are covered by a transparent external lens, the **cornea**. This lens enables, together with the **crystalline** lens, the production of a sharp image. The white part of the eye is the **sclera**. It forms the supporting wall of the eyeball and is continuous with the cornea.
Observing a cross-sectional view of the eyes it is possible to distinguish three layers:

1. the *external* layer composed by the sclera and cornea;

2. the *intermediate* layer in which there is the iris;

3. the *internal* layer, that is the sensory part of the eye, the retina.

In this work we will mainly focus on the last layer.

1.3 The retina

The **retina** is the site of transformation of light energy into a neural signal. It is a neural layer of approximately 0.5 mm thickness locating in the back of the eye, extending from the circular edge of the optic disc to the ora serrata [1].
The main structures identifiable in the retina, Figure 1.2, are the fovea and the optic disc. The **fovea** is a shallow depression with a horizontal diameter of approximately 1.5 mm . It has the highest concentration of cones in the retina and it is specialized for discrimination of detail and color vision. Within the fovea is a capillary-free zone 0.4 to 0.5 mm in diameter. The whole foveal area is considered the **macula** of human eye, recognizable as yellow pigmentation around the fovea. While the **optic disc**, or optic nerve head, is the site where ganglion cell axons accumulate and exit the eye. It is slightly elongated vertically with a horizontal and vertical diameter of 1.7 and 1.9 mm, respectively. The number of nerve fibers appears to be positively correlated with the size of the optic nerve head; larger discs have relatively more fibers than smaller discs. Smaller discs may demonstrate optic nerve head crowding. Fiber number decreases with age. It is paler than the surrounding retina because there is no retinal pigment epithelium (RPE), the outermost retinal layer.
Since the disc does not contain photoreceptor cells, light incident on the disc does not elicit a response; thus it represents the physiologic blind spot. We can recognize a depression in the surface of the disc, named the physiologic cup.

[2]https://webvision.med.utah.edu/book/part-i-foundations/simple-anatomy-of-the-retina/

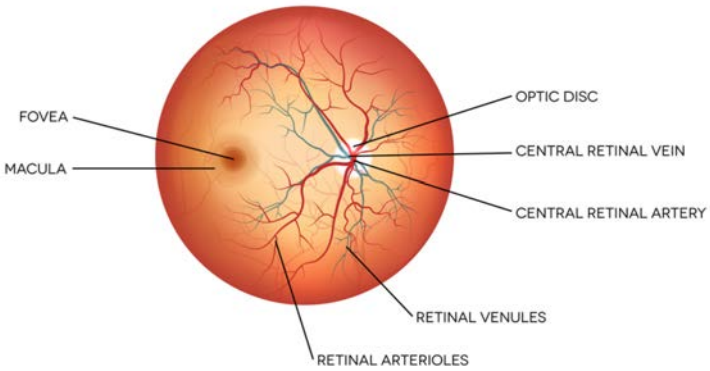

Figure 1.2: The retina

The retina has a complex and articulated **blood vessel network** that transports the oxigen. There are two sources of blood supply to the retina: the central retina artery and the choroidal blood vessels. The choroid receives the greatest blood flow (65-85%) and is vital for the maintainance of the outer retina, while the remaining 20-30% flows to the retina through the central retinal artery from the optic nerve head to nourish the inner retinal layers.

1.4 Why Retinal Image Analysis?

We can refer to *Retinal image analysis (RIA)* as the research field aimed at develop computer-aid methods for the study of the human retina.
The retina is the unique accessible part of the central nervous system (CNS) in vivo, so it can be possible studying systemic and neurological diseases.
It is thought that in some chronic disease changes in the retina can appear years before that other signs become evident. For this reason studying the retina could provide an useful mean to identify earlier a disease, prevent and assessing the efficacy of new treatments [2].
Among the diseases that can be studied via eye imaging and image analysis there are diabetes mellitus, hypertension, cardiovascular disease, etc.
Diabetes mellitus can have serious complication, such as diabetic retinopathy (DR). The retina should receive a constant supply of blood through a network of tiny blood vessels, over time, a persistently high blood sugar level can damage these blood vessels. If left undiagnosed and untreated it can lead to blindness [3]. Cardiovascular disease manifests itself in the retina in a number of ways. Hypertension and atherosclerosis, for example, cause changes in the ratio between the diameter of retinal the arteries and veins.
The retina shares with brain embriological origins, blood supply and nerve tissue so it is a site for biomarkers for microvascolature health and neurodegenerative damage. Moreover, retina is easier to image than the brain and with a far superior resolution [4]. Measuring geometric features of the vascular pattern visible in retinal imaging, such as vessels width, tortuosity, network branching, is a proxy for microvasculature health. For example, Alzheimer's

disease (AD) etiology includes cerebral small vessel disease. So the retina could be considered as a surrogate marker for microvascular pathology in AD.
For all these reasons the main purposes of RIA is detect retinal lesions, vessels and main landmarks. Computer-assisted methods measure variations or abnormalities in the retina that might be imperceptible or missed by a human grader, in an objective and repeatable way helping clinicians in risk-stratifying, diagnosis and assess therapies.
In the following two major techniques to acquire images of the fundus will be discussed.

1.5 Retinal imaging technologies

Retinal imaging takes a 2D digital picture of the 3D retinal surface. It is a patient-friendly tool that offers a non-invasive and inexpensive way to access the health of the CNS, a rich part of the microvasculature and a source of biomarkers for a lot of diseases.
The person being imaged is asked to sit and place his or her chin and forehead on a support to keep his or her head steady. Before proceeding, the instrument operator checks that the person is comfortable, adjusting the height of the instrument table if necessary. To the patient is asked to open the eyes as wide as possible and stare straight ahead at an object while a laser scans the eyes. In the following two common technologies, Figure 1.3, employed in our study, were described.

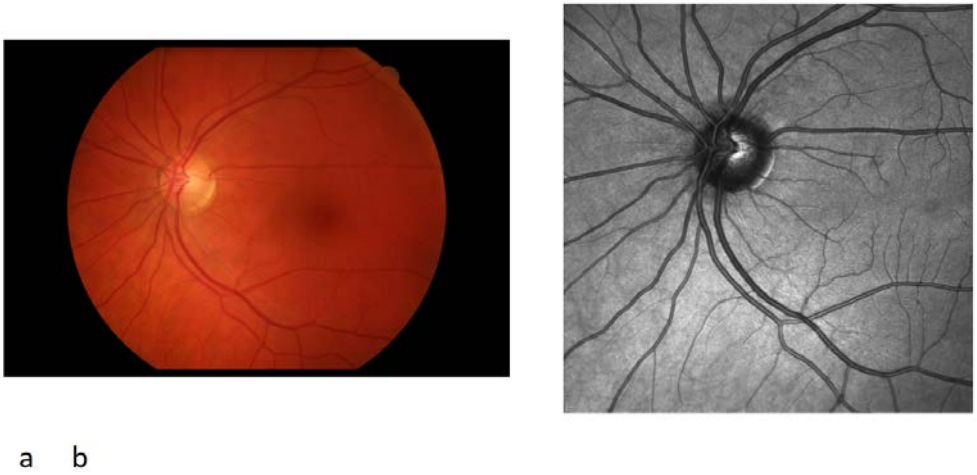

Figure 1.3: (a) Fundus camera image acquired with a Canon non-mydriatic camera and (b) scanning laser ophthalmoscope image acquired with a Heildelberg SPECTRALIS camera. The two images refer to the same retina, showing the difference in area viewable with the two devices.

1.5.1 Fundus camera imaging

A fundus camera is a specialized low power microscope with an attached camera[3]. Tipically field of view (FOV) graduations are between 20° and 50°. A larger FOV up to 60° can be achieved with special mydriatic camera for work with pupil dilation. Peripheral areas of the retina which lie outside the central FOV can be registered when the patient looks in different directions, changing the line of sight. With special Auto Mosaic (or Montage) software, the individual images can then be stitched together forming a panoramic image which can span an angular range of up to 110°.
The main advantages of this technique are the lower cost compared to other technologies, easy interpretation, full color (helping to distinguish between cupping and pallor), better detection of disc, hemorages, peripapillary atrophy etc. Disadvantages are the need of high light intensity for illumination of the retina and the fact that dilation of pupils often needed.
Fundus camera imaging is used in DR screening where it has been well validated as a screening Tool [5]. It is also used to monitoring changes in some retinal structures, for example changes in the optic nerve in conditions such as glaucoma.
The optic disc, on which rely this work, in this kind of images appears as a bright part with the highest radial (circular) symmetry, with high contrast between OD and vessels.

1.5.2 Scanning laser ophthalmoscope

It is a confocal imaging technique, that is, the retina is scanned point by point in a raster fashion by a focused laser beam and the reflected light is captured through a small aperture, the confocal pinhole.[4]
Unlike the fundus camera, the SLO are not capable of capturing full color images of the retina. However, the monochromatic laser illumination combined with a confocal optical system produce high-contrast finely detailed images.
Obtained images are typically rectangular with angle of view variable by instrument from 15–45°, comparable to fundus cameras, up to 200°, the so called *ultra-widefield*. The Heidelberg SPECTRALIS camera uses an infrared (IR) laser beam and confocal microscope arrangement to scan across the surface of the retina and form a fundus picture [4]. This particular SLO image at a slightly higher resolution than the fundus camera but captures a smaller area.
The SLO can be used to perform fluorescein angiography allowing for the measurement of capillary flow velocity, important in assessing the health of the microcirculation.
The cost and complexity of devices often see the SLO confined to research and ophthalmology clinics [2]. However, there are some advantages in the use of SLO over traditional fundus photography include improved image quality, patient comfort, video capability, and effective imaging of patients who do not

[3]https://www.opsweb.org/page/fundusphotography
[4]https://www.opsweb.org/page/SLO

dilate well, such as diabetics. The main applications are detecting biomarkers of diabetic retinopathy, as well as age-related macular degeneration [6].
Unlike in the fundus images, in the SLO image the OD appears as a dark elliptical shape part with high contrast between OD and background and low contrast between OD and vessels.

1.6 Aim and medical motivation of the thesis

The contribution of this work to RIA is the localization of the optic disc (OD) in scanning laser ophthalmoscope (SLO) images.
This project has been developed within the VAMPIRE[5] group at the University of Dundee.
The VAMPIRE (Vascular Assessment and Measurement Platform for Images of the REtina) software suite aims at providing efficient and reliable detection of retinal landmarks (optic disc, retinal zones, main vasculature), and quantify morphological features of the retinal vasculature. In the same context an alternative method to the one proposed in this thesis has been developed, which will be described in Section 3.6.
The location of the OD is important in retinal image analysis, to locate anatomical components in retinal images, for vessel tracking, as a reference length for measuring distances in retinal images, and for registering changes within the optic disc region due to disease [7].
The changes that occur in OD in terms of shape, color or depth of OD are indicators of different ophthalmic diseases. Severity of certain diseases, such as glaucoma and diabetic retinopathies can be measured with the change in the dimensions of OD. Glaucoma is the second leading cause of blindness, therefore diagnosing glaucoma at early stages is extremely important for an appropriate management of the medical treatment of the disease. In people with glaucoma damage the cup becomes larger in comparison to the optic disc, hence, the enlargement of the cup with respect to OD, measured as vertical cup-to-disc ratio (CDR), is one of the most important indicators of the disease [8].
The position and radius of the optic disc can be used also as the references for approximating fovea detection [9]. Moreover, it is crucial detecting the optic disc as initial step to identify the retinal zones.
Furthermore, the need of automatic procedure to locate the OD is foundamental since the definition of the optic disc is uncertaint itself. Histologically, what the clinicians sees as OD border has been source of controversia with the possibility that structures that most accurately define the boundary of the optic nerve head are not always visible by clinical examination techniques. It is thought that the OD rim depends on the 3D architecture of the Brunch's membrane and the underlying border tissue, rather than a single structure [10].

[5]https://vampire.computing.dundee.ac.uk/

1.7 Chapter summary

In this Chapter we have introduced the purpose of this thesis starting from a simple anatomical description of the eye and, in particular, of the retina. Giving a look at retinal imaging techniques used in our work and underlying the relevance of retinal image analysis.
The thesis, apart from Chapter 1 that is the introduction, has been divided in 6 more chapters as follows. In Chapter 2 the datasets and protocol for the annotations will be presented and in Chapter 3 a brief overview of the method existing in literature for locating the OD will be provided. In Chapter 4 all the theoretical tools useful to understand our works are reported, while the proposed methods are described in details in Chapter 5. At the end, in Chapter 6, the results of our methods compared to the annotators and to a validate algorithm implemented in the software VAMPIRE will be evaluated. Finally, in Chapter 7 we made our conclusions and some inspirations for future works.

Chapter 2

Materials

2.1 About this chapter

In this Chapter details on the materials, images and ground truth, used for our project are reported.
We will describe our datasets, images resolution and acquisition. Then we will deal with our annotations. Before going into details of what concerning the annotations, raters and protocol, we will briefly discuss on what is a validation process in retinal image analysis. At the end the strategy for testing our methods will be illustrated.

2.2 Datasets

In our study we used two datasets, one for algorithm development and one for performances evaluation. The first dataset consists of 20 SLO images; the second one is composed of 50 pairs of SLO and corresponding fundus camera images. The images were obtained in the context of the VAMPIRE collaboration between the Universities of Dundee and Edinburgh from the PREVENT Dementia study[1] from Edinburgh Imaging and the Edinburgh Clinical Research Facility. The SLO images were acquired with a Heildelberg SPECTRALIS SLO camera, the fundus images with a Canon non-mydriatic camera.
The SLO images are black and white images of resolution 1536x1536, while the coloured fundus images are of dimension of 2048x3072.
Unlike fundus images, there are no public datasets available for SLO images providing annotations on the optic disc.

2.3 Medical annotations

To validate an algorithm we need to have the ground truth (GT) to compare with. What 'to validate' means and how our GT have been generated will be explained in the following sub-sections.

[1] https://preventdementia.co.uk/.

2.3.1 Validating retinal image analysis algorithms

In a medical image processing context, validation can be defined as the '*process of showing that an algorithm performs correctly by comparing its output with a reference standard*' [11]. In medical image segmentation field, there is usually a lack of reference or 'gold' standard method. In many studies, the manual segmentation from expert raters is regarded as the gold standard. However, these manual denotation methods suffer from high inter-rater and intra-rater variability. An outline for validating automatic retinal image analysis algorithm is:

1. selecting a database such that it is a representative sample of the target population;

2. collecting annotations on the sample images;

3. running algorithms on the sample images;

4. comparing the output with the reference standard to assess the agreement between ground truth and the output of the algorithm.

The key task in validation is, hence, to assess qualitatively and quantitatively the agreement between automatic and manual measurements. A first point is defining how to declare agreement or not. In fact, a main issue with validation methodologies is the lack of standardization. Without standardization it remains difficult to compare the performances of different methods. Validation metrics should be chosen or defined according to their suitability to assess the outcome of the algorithm. This means that the metrics depend on the types of validation process. We can recognize four main types:

- *outcome orientated*, for example disease/no disease;

- *disease grading*, quantifying the severity of a pathology;

- *feature grading*, measurements of features in the image, for example tortuosity level of vessels;

- *image/pixel/measurement oriented*, locating structure in the image, measuring perimeter or area of a target region.

Particular attention should be paid in the process of generating the references standard. The two main issues are: the variability of expert judgement and the need for generating annotations directly comparable to the algorithm's output. By having several expert annotators the variability can be reduced. Moreover, a detailed protocol could minimize variations in the annotations as well as create annotations consistent with the algorithm's output.
We will dedicate the next sub-sections to the annotators and protocol for annotations.

2.3.2 Annotators and protocol for annotations

Four specialized ophthalmologists contributed to our research project, providing annotations: Dr. Andrew Tatham[2] consultant eye surgeon, Dr. Sirjhun Patel[3] ophthalmology registrar, Dr. Fraser Peck[3] ophthalmology registrar as well and Dr. Obaid Kousha[3] ophthalmic specialist trainee (Year 2).
The debate with these specialists revealed the uncertainty on the definition of the optic disc contour and the lack of standardization on how to draw the outline. This gives support to the importance of following an annotation protocol in collecting references in the context of image analysis, as said before.
We prepared a detailed protocol to annotate the images, also named 'Standing Operating Procedure' (SOP). To the annotators were asked to annotate all the 50 pairs of images independently. In details, they had to:

1. annotate with red coloured dots the OD contour;
2. in case of uncertain about some parts of the contour, annotate with yellow coloured dots this parts;
3. if present, annotate the Peripapillary Atrophy (PPA) with green coloured dots.

An example of annotation is displayed in Figure 2.1.

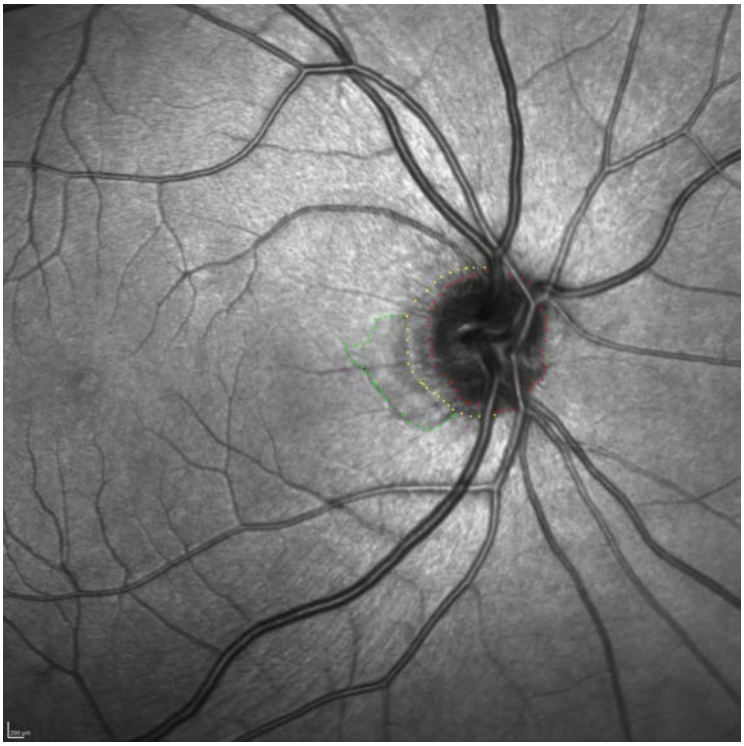

Figure 2.1: Example of annotation: red dots placed on the first choice of the contour, yellow dots along the second chosen contour, green dots on the PPA.

[2]Princess Alexandra Eye Pavilion, Chalmers Street, Edinburgh, EH3 9HA, UK.
[3]Department of Ophthalmology, NHS Tayside, Dundee, UK.

We asked also to re-annotate 15 images, SLO and fundus, randomly chosen among all the images to assess the annotators repeatability. In the case of an annotator on a test batch of nine images we found a problem concerning the intensity with which the contours were marked. This could be a problem when we extract the contour in automatic way. So we had recommended with all the annotators to make sure that every point has a good intensity since the colour intensities of the annotated points could vary, and some could be faint. On average, the doctors took 4-7 minutes to annotate an image. It is interesting to note that the annotators disagreed on which type of image was easier to annotate; some of them found easier to annotate the fundus images; others to annotate SLO images.
The original protocol designed for this annotation task is reported in Appendix on page 79.

2.4 Test planning

Our methods are aimed to locate one of the main landmark in the retina, the OD. So, in the validation process, we want to assess how much the two contours, automatic and manual, are similar. Common measurements to compare automatic segmentation and ground truth are metrics which quantify the spatial overlap between the two segmentations, like Dice or Jaccard, or point-to-point distances along the contours [11].
All our tests are conducted using three measurements to declare agreement: Dice coefficient, Jaccard coefficient and contour distance, explained in Section 4.4. First of all, to measure the spatial overlap we had to create a segmentation map from the contour manually drawn. Such maps are nothing but a binary image in which the optic disc has value equal to one and not optic disc is zero.
The comparisons, Section 6.4, are so structured:

- First proposed method compared to annotations on SLO images;
- Second proposed method compared to annotations on SLO images;
- Second proposed method compared to annotations on fundus images;
- VAMPIRE algorithm compared to annotations on fundus images.

Moreover we tested the inter- and intra-rater agreement, in Section 6.3.

2.5 Chapter summary

This chapter was included to highlight the challenges posed by the validation of retinal image algorithms. We wanted to define the way in which we collected the annotations and the strategies used to compare them with algorithm's outcome.
Now, before going into the explanation of our methods, we will present, in the next chapter, an *excursus* into the methodologies already proposed in literature for segmenting the optic disc.

Chapter 3

Related work for locating/segmenting the optic disc

3.1 About this chapter

The aim of this Chapter is to give an overview of the methods employed for the localization and segmentation of the optic disc, without claiming to be a detailed review. To our best knowledge, many optic disc detection studies have been presented on fundus camera images, while few on scanning laser ophthalmoscope images. For this reason we focused on methods designed for fundus images, aware of the differences in the OD's appearance in the two kind of images.
The existing papers mainly use features such as intensity, and shape to locate the position of the optic disc. Some robust methods are based on context, for example the presence of vascular structures and their orientation.
The methods for optic disc detection reviewed [12]-[14] in the literature can be divided in three main methodologies:

- Features-based

- Convergence of blood vessels

- Deformable-templates

In the following sections the three kind of strategies will be discussed (see Table 3.1 for a summary). Furthermore, the method implemented in the software VAMPIRE will be presented, since we are going to compare the performance of our methods with the performance of VAMPIRE. We decided not to investigate deep learning methods proposed in literature for OD location since our method is a non-learning approach. However, at the end of this chapter a deep learning approach developed in the same context of this thesis will be briefly illustrated.

3.2 Features-based approach

The features-based approach is less accurate than other two approaches and is less complex in time [14]. A features-based method is purely based on the properties of the optic disc, for example location, size, color and shape.
Sinthanayotim et al. [15] proposed an approach based on the intensity of the optic disc. They assume the OD's appearance as a yellowish region typically occupying approximately one seventh of the entire image.
The optic disc area is defined by the highest variation in intensity of adjacent pixels due to the variation in the appearance of dark blood vessels besides bright nerve fibres. The OD detection is essentially split into three different steps:

- pre-processing to enhance local contrast;
- determination of the variance within a running window;
- determination of the average variance within a running window.

This approach correctly detects the optic disc with the sensitivity and specificity of 99.1% on a local dataset consisting of 112 fundus images.
Abdullah et al. [16] presented an OD detection and segmentation methodology which is able to detect the OD centre without using any template or prior vascular information. The proposed method is based on morphological operations, the circular Hough transform and the grow-cut algorithm. To detect the OD centre, an initial morphological operation is conducted with the aim of enhance the OD and remove retinal vasculature and pathologies. Then the OD centre is approximated by a circular Hough Transform. Once localized the OD region, the grow-cut (GC) algorithm is employed to precisely segment the optic disc boundary. For the OD segmentation they use the detected OD centre point as the seed for the GC algorithm, which then iteratively searches for neighbours of initial seeds and expands the region based on the label and strength of each pixel. The method was evaluated on five public databases and one local. The algorithm achieves an optic disc detection success rate of 100% for these databases with the exception of 99.09% and 99.25% for the DRIONS-DB, MESSIDOR, and ONHSD databases, respectively. The optic disc boundary detection achieved an average spatial overlap of 78.6%, 85.12%, 83.23%, 85.1%, 87.93%, 80.1%, and 86.1% in DRIVE, DIARETDB1, CHASE_DB1, Shifa, DRIONS−DB1, MESSIDOR, and ONHSD databases, respectively.
Similary, Giraddi et al. [17] proposed a morphological approach. The method detects a first patch of the OD through a P-Tile thresholding. Then, making use of geometrical properties of the OD, i.e. area and eccentricity, they remove the false positive to avoid artefacts or pathologies. This step defines an initial patch of the OD for which centroid correction is computed. The final contour is performed by a GVF snake. The algorithm is robust and effective both in healthy images and pathological images, as well as in low contrast images. The performance, evaluated on three benchmark datasets, DIARETDB0, DIARETDB1, DRIVE, show an accuracy of 98%, 97% and 100%, respectively.

3.3 Convergence of blood vessels approach

These methods identify the optic disc as vessels convergence point and use the information provided by the vascular tree. The main issue with these methods is that they often require an accurate vessel segmentation, which is, in general, a difficult and time consuming task.
Hoover et al. [18] developed a voting-type algorithm called fuzzy convergence in order to detect the origination of the blood-vessel network (i.e. convergence point) which was considered as the centre of the OD in fundus image. The input to their algorithm was a binary segmentation of the blood vessels, in which each vessel was modelled by a fuzzy segment that contributed to a cumulative voting image. The output of the algorithm was a convergence image which was thresholded to identify the strongest point(s) of convergence. This technique successfully detects 89% of the normal and abnormal images in the STARE dataset.
Foracchia et al. [19] proposed a method exploiting the evidence that all retinal vessels originates from the OD and their path follows a similar directional pattern (parabolic course) in all images. To describe the general direction of retinal vessels at any given position in the image, a geometrical parametric model was built, where two of the model parameters are the coordinates of the OD centre. However, their approach is not just based on the detection of the area of the convergence of vessels but rather on the fitting of a model with respect to the entire vascular structure. To identify the model parameter, so OD centre, they minimizing the weighted residual sum of squares (RSS) by means of a simulated annealing optimization technique. The performance evaluation was assessed on 81 images of both normal and pathological subjects from STARE dataset. The OD position was correctly identifies in 79 out of 81 images (98%), even in rather difficult pathological situations.
In the same way X.Wu et al. [20], exploiting the vessels convergence, proposed a method based on several directional models: global, local and hybrid. They first built the global model, named the relaxed biparabola directional model, which rely on the evidence that the main vessels originates from the OD and their shape is a parabola. The global model is robust to pathologies and image artefacts. Then a local model, named the disc directional model, is built to characterize the local vessel convergence in the OD as well as the shape and the brightness of the OD. At the end the two models are combined to form a hybrid directional model to obtain a more robust OD localization. The method achieved accuracy of 100% on nine public datasets.
The method proposed by Perez-Rovira et al. [21] takes advantage of the spatial relationship between OD and main arcade to locate the OD. Two week detectors are used to locate independently the arcade and the OD. Without go into details, the main arcade detector chooses as vessel points the pixels having minimum intensity and that are fitted by Gaussian masks, exploiting the fact that the intensity profile along a short vessels segment can be approximated by inverted Gaussian. A simple OD detector seeks for a bright circular zone approximately centred vertically in the image, after smoothing the image to

remove noise and small bright spot. Then, OD candidates are detected as the peaks in the intensity level map and rated by their brightness.
Among all the possible pairs disc-arcades, the best pair including the OD is searched using a prior-knowledge and anatomical constraints. This algorithm fails in case of OD completely occluded, or due to the bad quality of the image. Sometimes the arcades were not fit well due to an abnormal tortuosity of vessels, while a circular lesion besides the OD is selected as OD.
The algorithm achieved a detection rate in public datasets grater than 90%, 91.4% in the STARE dataset, 95.0% in the DRIVE dataset, 96.7% in the DIARETDB1 dataset.

3.4 Deformable-templates approach

This is a template-matching method, in which the template is compared with the set of candidates to determine the best-matching candidates.
Model-based approach was proposed by Osareh et al. [22] to locate the OD centre. They created a gray-level template image by averaging the optic disc region of 25 images whose colors were normalized using histogram specifications. The OD was located by using the generated template calculating the normalized correlation coefficient to find the most similar match between the template and the image under consideration. This localization phase was followed by a snake fitting. They initialized the snake as a circle with a centre at the best-matched point obtained through template matching and with a circular diameter set to the width of the template. The method achieves an average accuracy of 90.32% in detecting the boundary of the optic disc of 75 images of the retina.
In a similar way, Wang et al. [23] employed a template matching method to approximately locate the optic disc centre. Then they applied the Level Set Method, which incorporates edge term, distance-regularization term and shape-prior term, to segment the shape of the optic disc. The performances of this method, evaluated on three public datasets, are comparable with the state-of-art methods.
Li and Chutatape [24] created an optic disc model (disc-space) by applying Principal Component Analysis (PCA) to a training set of 10 intensity normalized images that were manually cropped around the optic disc. The PCA is employed to the candidate regions to reduce the computation time. The candidate regions are defined by selecting and clustering the pixels with the highest 1% gray levels in intensity image. The proposed PCA approach includes three steps: obtaining disc space, projection on disc space, and calculating the distance from disc space. The PCA transformation is performed on the training set to obtain the disc-space. Then, the subimage is projected onto the disc-space and the distance from disc-space is simply defined as the Euclidean distance between the subimage and its reconstruction onto the disc space. To take into account size variations of the optic disc a multi-scale eigendisks is used. After the localization, a modified ASM method extracts the boundary of

the optic disc. In this work the optic disc was successfully detected in 99% of the images as the region with the smallest Euclidean distance to its projection onto the disc-space.
Dehghani et al. [25] suggested a method for localizing the OD by histogram matching. On a sample of images from the dataset they built a template for the optic disc. Instead of creating an image as template, they construct an histogram template for each color channel.
The template is obtained by averaging the histograms of each color channel for all retinal images sample. For localizing the OD a window is moved through the retinal image and in each sliding-window, they calculate the histograms of each channel. The correlation between the histograms in the moving window and the histograms of its corresponding channel in the template is computed. At the end the correlation is the weighted sum of the three correlation coefficients, one for each channel. A final thresholding on the correlation function is used to localize the centre of optic disc. The method was tested on two public datasets, DRIVE and STARE, and one local. The success rate was 100, 91.36, and 98.9, respectively.

Table 3.1. Table to summarize the reviewed papers

	Authors	Data sets	Accuracy
Features-based	Sinthanayotim et al. [15]	Local	99.1%
	Abdullah et al. [16]	DRIVE, DIARETDB1, CHASE_DB1, DRIONS-B1, MESSIDOR, ONHSD, local	78.6%, 85.12%, 83.23%, 87.93%, 80.1%, 86.1%, 85.1%.
	Giraddi et al. [17]	DIARETDB0, DIARETDB1, DRIVE	98%, 97%, 100%
Convergence of blood vessels	Hoover et al. [18]	STARE	89%
	Foracchia et al. [19]	STARE	98%
	X.Wu et al. [20]	STARE, ARIA, MESSIDOR, DIARETDB0, DIARETDB1, DRIVE, ROC, ONHSD , DRIONS	100% (localization)
	Perez-Rovira et al. [21]	STARE, DRIVE, DIARETDB1	91.4%, 95.0%, 96.7%
Deformable-templates	Osareh et al. [22]	Local	90.32%
	Wang et al. [23]	DRIVE, DIARETDB1 DIARETDB0	88.17%, 88.16% 89.06% (overlap)
	Li and Chutatape [24]	Local	99% (localization) 94% (boundary detection)
	Dehghani et al. [25]	DRIVE, STARE, local	100%, 91.36%, 98.9%

3.5 The method implemented in VAMPIRE

The method proposed by Giachetti et al. [26], Figure 3.1, is implemented in the software suite for the semi-automatic quantification of retinal vessel properties from fundus camera images (VAMPIRE). The approach is based on OD's appearance, i.e. its shape and brightness, combined with the contextual information. The method separates the location and the segmentation tasks. The OD location is performed using a simple probabilistic approach based on combining the output of simple detectors, one related to radial symmetry and the other related to vessel density. The assumption behind this technique is that the OD centre is located where the vessel density is high. A key point is that the OD searching and segmentation is performed on impainted images obtained by removing the vessel mask and propagating neighboring information in the masked region. The iterative procedure for obtaining the impainted image is:

1. remove vessel pixel from the image. Select the border set composed of the empty pixels close to valued ones;

2. for each border pixel, compute the median of the valued pixel in a 5x5 neighborhood and fill the pixel with this value;

3. recompute the border set and iterate until it is empty.

The segmentation consists of the fitting of incrementally complex contour models at increasing image resolutions. At the coarsest resolution the fitting model is a circle, that will be explained in Section 5.2.3. Increasing the resolution a vertical elongation term is added and, at the highest resolution, a rotation term is added so that the final OD is a generic ellipse. At the end a snake runs to refine the contour. The method can provide accurate results both in term of optic disc location and contour segmentation accuracy, with an average error reasonably close to the interoperator errors.

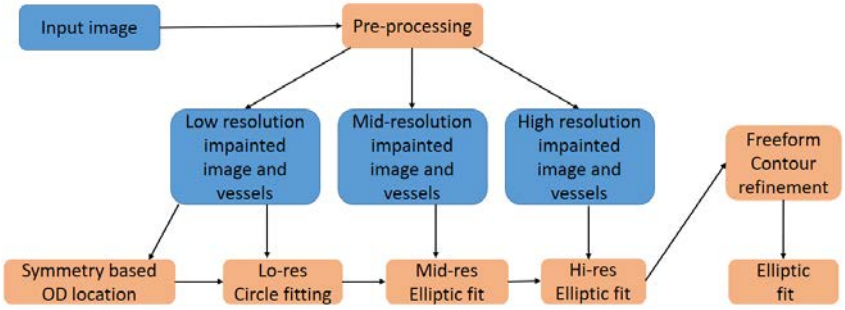

Figure 3.1: Flow chart of the method showing the steps of the multiscale optic disc localization and segmentation.

3.6 A deep learning approach

A deep learning approach, presented in [27], has been developed in parallel with the method proposed in this thesis within the same context.
The pipeline of the algorithm, Figure 3.2, can be divided in: Locating/detecting, ROI extraction and final segmentation.

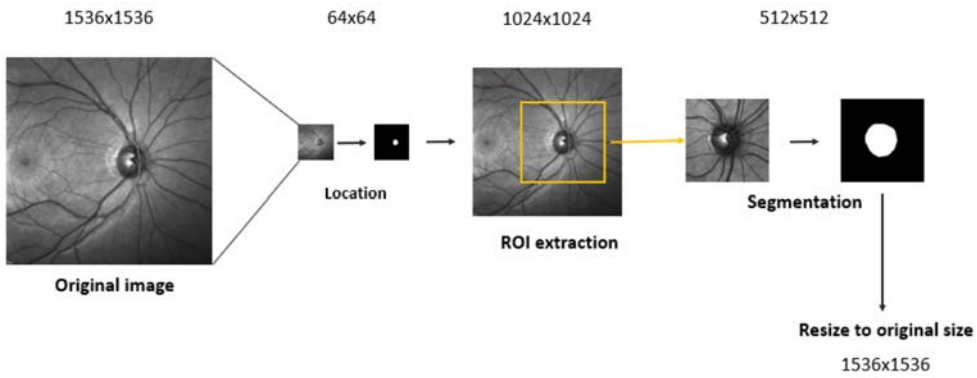

Figure 3.2: Pipeline of the method. (Image taken from [27])

Locating/detecting

In this stage a classifier locates the optic disc in low-resolution images of dimension 64x64. The classifier is composed of four different CNNs (A, B, C, D), combined to obtain a single binary map. The first three networks are designed for pixel-wise classification, share the same architecture and same training set. Such nets differ only in the initialization of the weights. The D-net is designed for region-wise classification of output size 4x4. It is useful to individualize the region in which the OD is. The resulting segmentation map is the AND (pixel-wise) of the segmentation maps resulting from each net.

ROI extraction

From the segmentation map found at the previous step, the centre of the optic disc is calculated as the barycentre of the point classified as OD.
From the original SLO images, downsized at resolution of 512x512, a ROI of 256x256 is extracted around the predicted OD centre.

Final segmentation

The main strategy used in this step is the transfer learning, to exploit as much information as possible. The classifier was at first trained on 70 images in which the ground truth are1 the segmentation maps produced by the algorithm proposed in the method '*Hand-crafted features for OD contour points selection*', Section 5.3. In the second phase the trained network is re-trained on the image annotated by expert ophthalmologists.
The classifier for the final segmentation is inspired by the U-net architecture, with 52 layers and "dice-pixel-classification" as output layer.

3.7 Chapter summary

After giving an overview of some representative methodologies existing in literature, summarized in the table 3.1, we can move towards the discussion of our proposed methods. For a better understanding, in the next Chapter, the theoretical tools behind our work are illustrated briefly.

Chapter 4

Theoretical tools

4.1 About this chapter

In this Chapter we provide a brief explanation of the theoretical instruments lying behind the methods, as well as the evaluation measurements used in the testing phase.
We organized all the methods in three main categories:

- **Numerical mathematics** in which we can find the *Bisection root findings method* used to automatically select a threshold for the initial segmentation in Section 5.2.1, the *Nelder-Mead simplex method* that is the optimizer chosen in the circle fitting of Section 5.2.3 and the *Ellipse fitting*, the approach used to approximate the resulting segmentation with an ellipse, Section 5.2.6.

- **Image processing** in which a brief overview of *Morphological image processing* is given to better understand our methods in next Chapter, *Non parametric smoothing* utilized to obtain a smoother and finer contour in Section 5.3.4 and basic concepts of *Image registration* to understand our approach to register fundus and SLO images, in Section 6.2.

- **Quantitative measurements** in which we defined both *Similarity measurements*, Dice and Jaccard coefficients, and *Distance measurement*, point-to-point distance between two contours. These quantitative measurements are used in the testing phase in Chapter 6.

In the following sections these categories will be discussed.

4.2 Numerical mathematics

4.2.1 Bisection root findings method

The bisection method is a root-finding method that applies to any continuous functions.
Let $f(x)$ continuous in the interval $[l, r]$ and $f(l)f(r) < 0$ then a zero of the

function, α, is in (l, r).
The method consists of repeatedly bisecting the interval defined by the values l and r and then selecting the subinterval in which the function changes sign, and therefore must contain a root. Here the pseudocode

Algorithm 1 Bisection Method

```
k=0
while the interval (l^(k), r^(k)) is 'big enough' do
    c = (l^(k) + r^(k)) / 2
    x^(k) = c
    if f(c)f(r^(k)) > 0 then
        this means that α is between l^(k) and c, so set r^(k+1) = c and l^(k+1) = l^(k)
    else
        this means that α is between c and r^(k) so set l^(k+1) = c and r^(k+1) = r^(k)
    end if
    k = k+1
end while
```

4.2.2 Nelder-Mead simplex method

The Nelder-Mead simplex algorithm [28] is a method proposed for minimizing a real-valued function $f(\mathbf{x})$ for $\mathbf{x} \in R^n$

The Nelder-Mead method is simplex-based. A *simplex* is a geometric figure in R^n that is the convex hull of $n+1$ vertices $\mathbf{x}_1, \ldots \mathbf{x}_{n+1} \in R^n$. For example, Figure 4.1, a simplex in R^2 is a triangle, and a simplex in R^3 in a tetrahedron.

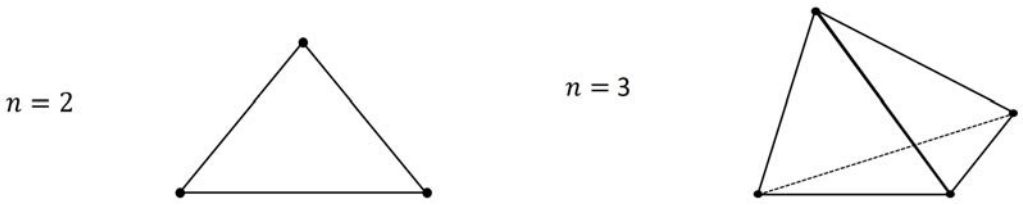

Figure 4.1: Simplex for $n = 2$ is a triangle, for $n = 3$ is a tetrahedron.

To define a complete Nelder-Mead method four scalar parameters must be specified: coefficients of *reflection* (ρ), *expansion* (χ), *contraction* (γ) and *shrinkage* (σ). These parameters should satisfy

$$\rho > 0,\ \chi > 1,\ \chi > \rho,\ 0 < \gamma < 1 \text{ and } 0 < \sigma < 1. \tag{4.1}$$

The standard configuration of these parameters is

$$\rho = 1,\ \chi = 2,\ \gamma = \frac{1}{2} \text{ and } \sigma = \frac{1}{2}. \tag{4.2}$$

A simplex direct search method begins with a set of $n+1$ points $\mathbf{x}_1, \dots \mathbf{x}_{n+1} \in R^n$ that are considered as the vertices of a simplex S, and the corresponding set of function values at the vertices $f_j := f(\mathbf{x}_j)$, for $j = 1, \dots, n+1$. The initial simplex S has to be nondegenerate, i.e., the points $\mathbf{x}_1, \dots \mathbf{x}_{n+1}$ must not lie in the same hyperplane.

Statement of the algorithm. At the beginning of the kth iteration, $k \geqslant 0$, a nondegenerate simplex Δ_k is given, along with its $n+1$ vertices, each of which is a point in R_n. It is always assumed that iteration k begins by ordering and labeling these vertices as $\mathbf{x}_1^{(k)}, \dots, \mathbf{x}_{n+1}^{(k)}$, such that

$$f_1^k \leqslant f_2^k \leqslant \cdots \leqslant f_{n+1}^k, \tag{4.3}$$

where f_1^k denotes $f(\mathbf{x}_1^{(k)})$. The kth iteration generates a set of $n+1$ vertices that define a different simplex for the next iteration, so that $\Delta_{k+1} \neq \Delta_k$. We refer to $\mathbf{x}_1^k$ as the best point or vertex, to $\mathbf{x}_{n+1}^k$ as the worst point, and to $\mathbf{x}_n^k$ as the next-worst point. In the same way we refer to f_{n+1}^k as the worst function value and so on.
The result of each iteration is either a single new vertex, that replaces $\mathbf{x}_{n+1}$ in the set of vertices for the next iteration, or in case of shrink, a set of new points that, together with $\mathbf{x}_1$ form the simplex at the next iteration.

One iteration of Algorithm NM

1. **Order**. Order the $n+1$ vertices to satisfy 4.3.

2. **Reflect**. Compute the *reflection* point $\mathbf{x}_r$ from

$$\mathbf{x}_r = \bar{\mathbf{x}} + \rho(\bar{\mathbf{x}} - \mathbf{x}_{n+1}) = (1+\rho)\bar{\mathbf{x}} - \rho\mathbf{x}_{n+1}, \tag{4.4}$$

   where $\bar{\mathbf{x}} = \sum_{i=1}^{n} \mathbf{x}_i/n$ is the centroid of the n best points (all vertices except $\mathbf{x}_{n+1}$). Evaluate $f_r = f(\mathbf{x}_r)$.
   If $f_1 \leqslant f_r < f_n$, accept the reflected point $\mathbf{x}_r$ and terminate the iteration.

3. **Expand**. If $f_r < f_1$, calculate the *expansion* point $\mathbf{x}_e$

$$\mathbf{x}_e = \bar{\mathbf{x}} + \chi(\mathbf{x}_r - \bar{\mathbf{x}}) = \bar{\mathbf{x}} + \rho\chi(\bar{\mathbf{x}} - \mathbf{x}_{n+1}) = (1+\rho\chi)\bar{\mathbf{x}} - \rho\chi\mathbf{x}_{n+1}, \tag{4.5}$$

   and evaluate $f_e = f(\mathbf{x}_e)$. If $f_e < f_r$, accept $\mathbf{x}_e$ and terminate the iteration, otherwise accept $\mathbf{x}_r$ and terminate the iteration.

4. **Contract**. If $f_r \geqslant f_n$, perform a contraction between $\bar{\mathbf{x}}$ and the better of $\mathbf{x}_{n+1}$ and $\mathbf{x}_r$.

   a **Outside**. If $f_n \leqslant f_r < f_{n+1}$, perform an outside contraction

$$\mathbf{x}_c = \bar{\mathbf{x}} + \gamma(\mathbf{x}_r - \bar{\mathbf{x}}) = \bar{\mathbf{x}} + \gamma\rho(\bar{\mathbf{x}} - \mathbf{x}_{n+1}) = (1+\rho\gamma)\bar{\mathbf{x}} - \rho\gamma\mathbf{x}_{n+1}, \tag{4.6}$$

   and evaluate $f_c = f(\mathbf{x}_c)$. If $f_c \leqslant f_r$, accept $\mathbf{x}_c$ and terminate the iteration; otherwise, perform a shrink (step 5).

b **Inside**. If $f_r \geqslant f_{n+1}$, perform an inside contraction

$$\mathbf{x}_{cc} = \bar{\mathbf{x}} - \gamma(\bar{\mathbf{x}} - \mathbf{x}_{n+1}) = (1-\gamma)\bar{\mathbf{x}} + \gamma\mathbf{x}_{n+1}, \tag{4.7}$$

and evaluate $f_{cc} = f(\mathbf{x}_{cc})$. If $f_{cc} < f_{n+1}$, accept $\mathbf{x}_{cc}$ and terminate the iteration; otherwise go to step 5.

5. **Perform a shrink step**. Evaluate f at the n points $\mathbf{v}_i = \mathbf{x}_1 + \sigma(\mathbf{x}_i - \mathbf{x}_1),\ i = 2, \ldots, n+1$. The vertices of the simplex at the next iteration consist of $\mathbf{x}_1,\ \mathbf{v}_2, \ldots, \mathbf{v}_{n+1}$.

The idea is to try to expand the simplex if good values of the objective function are found, contract otherwise. In Figure 4.2, are shown the effects of reflection. expansion, contraction and shrinkage for a simplex in two dimensions with the standard values for the four coefficients (4.2).

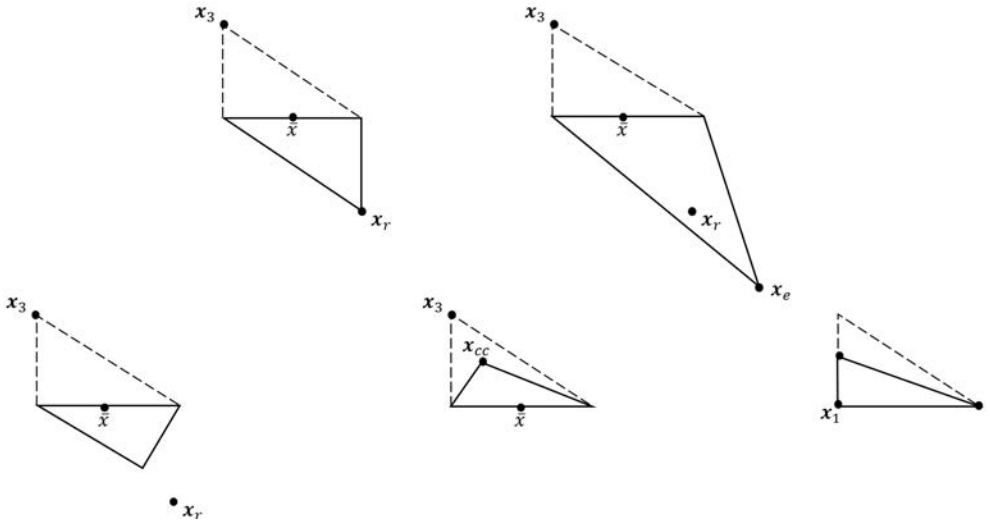

Figure 4.2: NM operations: reflection $\mathbf{x}_r$ expansion $\mathbf{x}_e$, inside contraction $\mathbf{x}_c$, outside contraction $\mathbf{x}_{cc}$ and a shrink.

4.2.3 Ellipse fitting

In this Section the method proposed by A.Fitzgibbon et al. [29] for fitting ellipses to segmented data is discussed.

Problem statement Let $\mathbf{a} = [a\ b\ c\ d\ e\ f]^T$ parameter vector and $\mathbf{x} = [x^2\ xy\ y^2\ x\ y\ 1]^T$,

$$F(\mathbf{a},\mathbf{x}) = \mathbf{a}\cdot\mathbf{x} = ax^2 + bxy + cy^2 + dx + ey + f = 0 \tag{4.8}$$

is a general conic represented by an implicit second order polynomial. $F(\mathbf{a},\mathbf{x})$ is called the "algebraic distance" of a point (x, y) to the conic $F(\mathbf{a},\mathbf{x}) = 0$. The fitting of a general conic may be approached by minimizing the sum of squared algebraic distances

$$D_A(\mathbf{a}) = \sum_{i=1}^{N} F(\mathbf{x}_i)^2 \tag{4.9}$$

of the curve to the N data points $\mathbf{x}_i$.
The parameter vector $\mathbf{a}$ has to be constrained in some way in order to avoid the trivial solution $\mathbf{a} = 0$ and to take into account that any multiple of a solution $\mathbf{a}$ represents the same conic.
The appropriate constraint so that the conic is forced to be an ellipse is that the discriminant $b^2 - 4ac < 0$. However this constraint problem is difficult to solve in general. The constraint $4ac - b^2 = 1$ can be regarded as a "normalized" version of the elliptical constraint $b^2 - 4ac < 0$, as $\mathbf{a}$ is only defined up to a scale factor. This is a quadratic constraint, in matrix form $\mathbf{a}^T\mathbf{C}\mathbf{a} = \mathbf{1}$ as

$$\mathbf{a}^T \begin{bmatrix} 0 & 0 & 2 & 0 & 0 & 0 \\ 0 & -1 & 0 & 0 & 0 & 0 \\ 2 & 0 & 0 & 0 & 0 & 0 \\ 0 & 0 & 0 & 0 & 0 & 0 \\ 0 & 0 & 0 & 0 & 0 & 0 \\ 0 & 0 & 0 & 0 & 0 & 0 \end{bmatrix} \mathbf{a} = \mathbf{1} \tag{4.10}$$

Problem 4.9 becomes

$$\textit{minimizing } E = \| \mathbf{D}\mathbf{a} \|^2 \textit{ subject to the constraint } \mathbf{a}^T\mathbf{C}\mathbf{a} = \mathbf{1} \tag{4.11}$$

where the design matrix $\mathbf{D}$ is defined as in 4.9. By introducing the Lagrange multiplier λ and differentiating, we get a system of equations

$$\begin{aligned} &2\mathbf{D}^T\mathbf{D}\mathbf{a} - 2\lambda\mathbf{C}\mathbf{a} = 0 \\ &\mathbf{a}^T\mathbf{C}\mathbf{a} = \mathbf{1} \end{aligned} \tag{4.12}$$

This system can be rewritten as

$$\mathbf{S}\mathbf{a} = \lambda\mathbf{C}\mathbf{a} \tag{4.13}$$

$$\mathbf{a}^T\mathbf{C}\mathbf{a} = \mathbf{1} \tag{4.14}$$

where S is the scatter matrix $\mathbf{D}^T\mathbf{D}$. This system is solved by considering the generalized eigenvectors of 4.13: if (λ_i, u_i) solves 4.13, then so does $(\lambda_i, \mu u_i)$ for any μ. Starting from 4.14 it is possible to evaluate μ_i as $\mu_i^2\mathbf{u}_i^T\mathbf{C}\mathbf{u}_i = 1$, giving

$$\mu_i = \sqrt{\frac{1}{\mathbf{u}_i^T\mathbf{C}\mathbf{u}_i}} = \sqrt{\frac{1}{\mathbf{u}_i^T\mathbf{S}\mathbf{u}_i}}. \tag{4.15}$$

The solution of 4.12 is found by setting $\hat{\mathbf{a}}_i = \mu_i\mathbf{u}_i$

It can be shown that the minimization of $\| \mathbf{D}\mathbf{a} \|^2$ subject to $4ac - b^2 = 1$ yields exactly one solution, which corresponds to an ellipse, due to the constraint itself. This method has some interesting advantages: is ellipse-specific, also under noise conditions; invariance to affine transformation of the data; high robustness to noise; and high computational efficiency.

4.3 Image processing

4.3.1 Morphological image processing

In the context of *mathematical morphology* we can refer to the word *morphology* as a tool for extracting image components that are useful in the representation and description of region shape, such as boundaries, skeletons and complex hull [30]. The language of mathematical morphology is set theory. The applications based on the morphological concepts discussed in this section involve binary images. In this case, the logic operations are performed on a pixel by pixel basis between corresponding pixels of two or more images (except NOT).

Dilation

Let A and B be set in Z^2, the *dilation* of A by B, denoted $A \oplus B$, is defined as

$$A \oplus B = \{z \mid (\hat{B})_z \cap A \neq \oslash\}. \tag{4.16}$$

The dilation of A by B is the set of all displacements, z, such that $\hat{B}$ and A overlap by at least one element. Set B is commonly named as the *structuring element* in dilation, as well as in other morphological operations. An intuitive application of dilation is bridging gaps.

Erosion

Let A and B be set in Z^2, the *erosion* of A by B, denoted $A \ominus B$, is defined as

$$A \ominus B = \{z \mid (B)_z \subseteq A\}, \tag{4.17}$$

that means that the erosion of A by B is the set of all points z such that B, translated by z, is contained in A. A simple use of erosion is to eliminate irrelevant detail (in terms of size) from a binary image.
Dilation and erosion are duals of each other with respect to set complementation and reflection. That is, $(A \ominus B)^c = A^c \oplus \hat{B}$.

By combining this two operations in different way we obtain other operations, opening and closing.

Opening and Closing

The *Opening* of set A by structuring element B, denoted $A \circ B$, is defined as the erosion of A by B, followed by a dilation of the result by B:

$$A \circ B = (A \ominus B) \oplus B. \tag{4.18}$$

This operation generally smoothes the contour of an object, breaks narrow isthmuses, eliminates thin protrusions and deletes noisy pixels from binary images.

The opening operation has a simple geometric interpretation, Figure 4.3. Suppose that we consider the structuring element B as a flat "rolling ball", that is rolled around inside the boundary of A. The boundary of $A \circ B$ is fixed by the points of B that reach the farthest into the boundary of A. So we can consider the opening result as the union of all translations of the structuring element B that fit into the image A. That is, opening can be expressed as a fitting process such that

$$A \circ B = \cup\{(B)_z \mid (B)_z \subseteq A\}. \tag{4.19}$$

The *Closing* of set A by structuring element B, denoted $A \bullet B$, is defined as the dilation of A by B, followed by the erosion of the result by B.

$$A \bullet B = (A \oplus B) \ominus B \tag{4.20}$$

This operation also tends to smooth contours but it generally fuses narrow breaks and long thin gulfs, eliminates small holes and fills gaps in the contour. Closing has a similar geometric interpretation, except that the structuring element B is now rolled on the outside of the boundary, Figure 4.4.

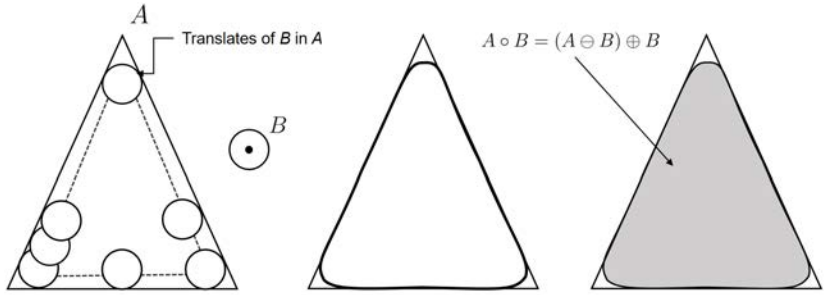

Figure 4.3: (a) Structuring element B "rolling" along the inner boundary of A (the dot indicates the origin of B). (c) The heavy line is the outer boundary of the opening. (d) Complete opening (shade).

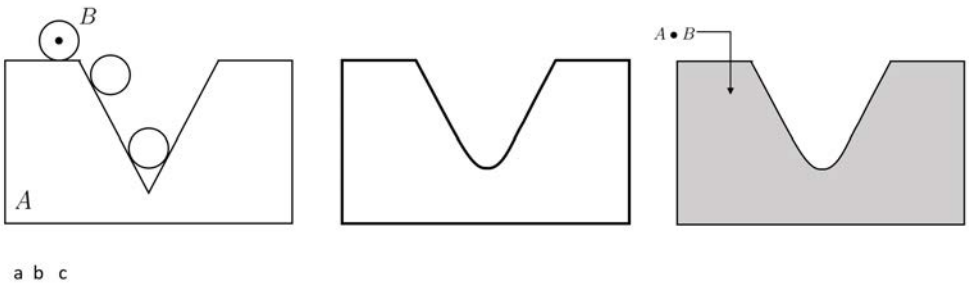

Figure 4.4: a) Structuring element B "rolling" on the outer boundary of set A. (b) The heavy line is the outer boundary of the closing. (d) Complete opening (shade).

As in the case of dilation and erosion, opening and closing are duals of each other with respect to set complementation and reflection. That is, $(A \bullet B)^c = (A^c \circ \hat{B})$. The opening operation satisfies the following properties:

(i) $A \circ B$ is a subset (subimage) of A.

(ii) If C is a subset of D, then $C \circ B$ is a subset of $D \circ B$.

(iii) $(A \circ B) \circ B = A \circ B$.

Likewise, the closing operation satisfies the properties:

(i) A is a subset (subimage) of $A \bullet B$.

(ii) If C is a subset of D, then $C \bullet B$ is a subset of $D \bullet B$.

(iii) $(A \bullet B) \bullet B = A \bullet B$.

4.3.2 Adaptive thresholding

Thresholding is the simplest approach of segmentation used to create a binary image from greyscale or coloured images, as shown in Figure 4.5.

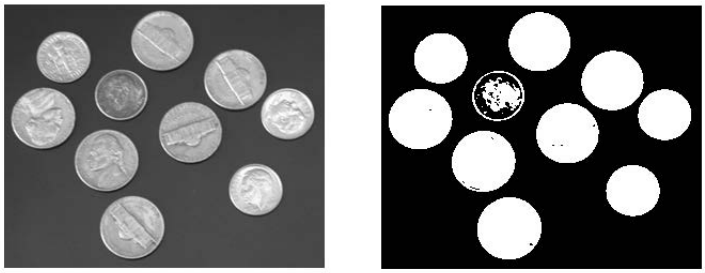

Figure 4.5: The input image (a) converted into binary image using a single threshold (b).

The working principle of the approach is selecting a threshold value for assigning colors below ad above thresholds, to get the segmented image. Pixels are partitioned depending on the intensity values of pixels: replace each pixel in an image with a black pixel if the image intensity $I_{i,j}$ is less than some fixed constant T (that is, $I_{i,j} < T$), or a white pixel if the image intensity is greater than that constant.
Thresholding may be seen as an operation that involves tests against a function T of the form

$$T = T[x, y, p(x, y), f(x, y)] \tag{4.21}$$

where f(x,y) is the gray level of point (x, y) and $p(x, y)$ denotes some local property of this point. A thresholded image $g(x, y)$, with a single threshold, Figure 4.6 (a), is defined as

$$g(x,y) = \begin{cases} 1, \ if \ f(x,y) > T \\ 0, \ if \ f(x,y) \leqslant T \end{cases} . \tag{4.22}$$

Pixels labeled 1 correspond to objects whereas pixels labeled 0 correspond to background. But multi-thresholding, Figure 4.6 (b), with appropriate thresholds $T1$ and $T2$ is given as

$$g(x,y) = \begin{cases} a, \ if \ f(x,y) > T2 \\ b, \ if \ T1 < f(x,y) \leqslant T2 \\ c, \ if \ f(x,y) \leqslant T1 \end{cases} \tag{4.23}$$

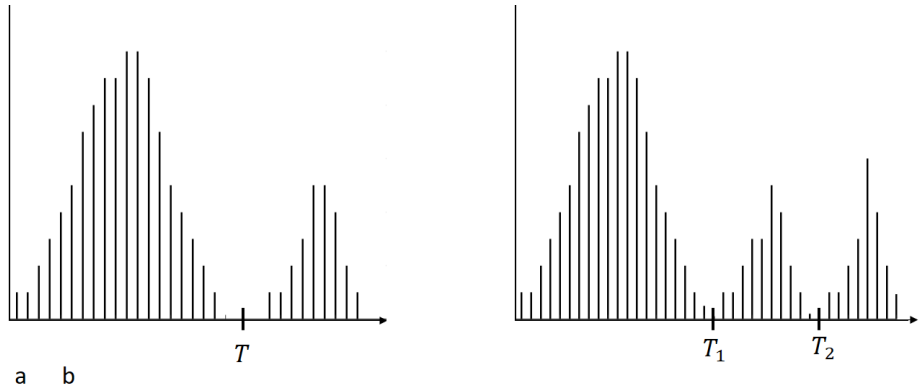

Figure 4.6: Gray-level histograms that can be partitioned by (a) a single threshold, and (b) multiple thresholds.

- if T depends only on $f(x, y)$ the threshold is called *global*;
- if T depends on both $f(x, y)$ and $p(x, y)$, the threshold is called *local*;
- if T depends on the spatial coordinates x and y, the threshold is called *dynamic* or *adaptive*.

A basic approach to adaptive thresholding is to divide the original image into subimages and then utilize a different threshold to segment each subimage. The key issues in this approach are how to subdivide the image and how to estimate the threshold for each resulting subimage.

4.3.3 Non-parametric smoothing

In smoothing problem the signal u_k has to be reconstructed starting from the discrete observations y_k. Let's suppose to have signal $y(t)$ sampled on a sampling grid Ω_s, infrequent and non-uniform. We want to estimate the signal

on a "virtual" grid Ω_v, uniform and finer than the sampling grid.
Our model of the measure is

$$y = Gu + v \tag{4.24}$$

where y is the signal (dimension n), G is a "quasi-Toeplitz" matrix (nxN), u is the signal we want to estimate (dimension N) and v (dimension n) is the uncertainty on the measures y [31]. The matrix G is obtained by deleting from the matrix $G_v = I_N$ the rows corresponding to the missing samples.
Assuming that the covariance matrix of v is $\Sigma_v = \sigma^2 B$, where B is a known positive definite matrix and σ^2 is a scalar. The estimate $\hat{\mathbf{u}}$ is defined as

$$\hat{\mathbf{u}} = \underset{\mathbf{u}}{\operatorname{argmin}}\{(\mathbf{y} - \mathbf{G}\mathbf{u})^T \mathbf{B}^{-1}(\mathbf{y} - \mathbf{G}\mathbf{u}) + \gamma \mathbf{u}^T \Sigma_u^{-1} \mathbf{u}\} \tag{4.25}$$

where $\gamma > 0$ is the so called *regularization* parameter and $\Sigma_u^{-1} = \mathbf{F}^T\mathbf{F}$, where $\mathbf{F} = \mathbf{\Delta}^m$ and $\mathbf{\Delta}$, NxN Toeplitz matrix lower triangular with first coloumn $(-1, -1, 0, \ldots, 0)^T$:

$$\mathbf{\Delta} = \begin{bmatrix} 1 & 0 & 0 & 0 & 0 \\ -1 & 1 & 0 & 0 & 0 \\ 0 & -1 & 1 & 0 & 0 \\ \cdots & \cdots & \cdots & \cdots & \cdots \\ 0 & \cdots & \cdots & -1 & 1 \end{bmatrix}, \quad \mathbf{F} = \mathbf{\Delta}^m \tag{4.26}$$

The matrix $\mathbf{F}$ penalizes the $m-$differences; increasing m leads to smoother solutions. For $m = 2$, the matrix F is

$$\mathbf{F} = \begin{bmatrix} 1 & 0 & 0 & 0 & \cdots & 0 \\ -2 & 1 & 0 & 0 & \cdots & 0 \\ 1 & -2 & 1 & 0 & \cdots & 0 \\ \cdots & \cdots & \cdots & \cdots & \cdots & \cdots \\ 0 & \cdots & \cdots & 1 & -2 & 1 \end{bmatrix}.$$

The first term on the right-hand side in 4.25 measures the fidelity to the data, whereas the second term is introduced to penalize the roughness of the estimate. The regularization parameter γ determines the relative weight between the fidelity to experimental data and the smoothness of the solution. If γ is too small, the regularization effect vanishes and the solution is an interpolation of the data. On the other hand, too large values of γ produce smooth estimates that may be unable to track sharp variations in the true input (over-smoothing). For a better understanding of the effect of the parameter γ refer to Figure 4.7.
It is possible to demonstrate that problem 4.25 has a closed form solution:

$$\hat{\mathbf{u}} = (\mathbf{G}^T\mathbf{B}^{-1}\mathbf{G} + \gamma\mathbf{F}^T\mathbf{F}^{-1})\mathbf{G}^T\mathbf{B}^{-1}\mathbf{y}. \tag{4.27}$$

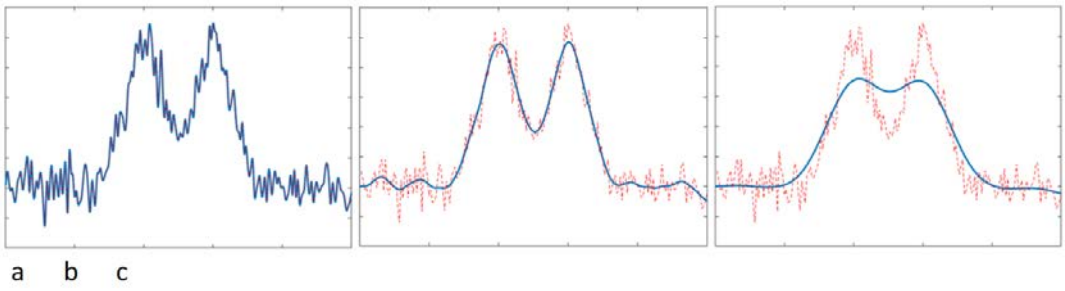

Figure 4.7: An example of smoothing of a biological signal at increasing value of gamma, from left to right. Red dashed line is the noisy signal, blue line is the smoothed estimate signal. For very low value of γ (a) the estimated $\hat{\mathbf{u}}$ 4.27 follows the noisy data, while for high value the estimate is too regular.

4.3.4 Image Registration

Registration is the process of determining a one-to-one mapping or transformation between the coordinates in one space and those in another, such that points in the two spaces that correspond to the same anatomical point are mapped to each other.
From an operational view, the inputs of registration are the two images to be registered; the output is a geometrical transformation, which is merely a mathematical mapping from points in one image to points in the second.
In Figure 4.8 an example of multi-modal registration.

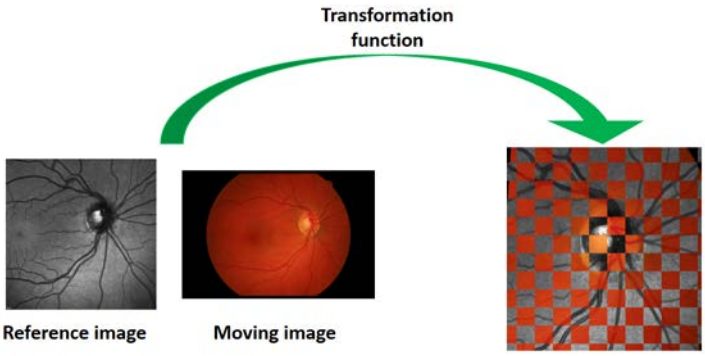

Figure 4.8: Multi-modal registration between SLO and fundus images.

Registration can be classified according to the image acquisition modality. Registration between like modalities is called 'intramodal' or 'monomodal'; registration between differing modalities is called 'intermodal' or 'multimodal' registration. Similarly, registration between image of the same patient is 'intrapatient', between different patient 'interpatient'.
The image to not be modified is called *reference* image or *fixed* image; the image to be transformed into alignment with the reference image is called *target* image or *moving* image. The *transformation function* is the function used to modify the target image to overlap the reference.

We can formalize the problem as following: given n corresponding points in two images of the same scene, $[(X_i, Y_i),\ (x_i, y_i)],\ i = 1, \ldots, n$, determine functions

$$X = f(x, y)$$
$$Y = g(x, y)$$

that will register the images. We will refer to image with coordinates (x, y) as the reference image and the image with coordinates (X, Y) as the moving image.
In the following subsections we briefly report the two mapping functions used to register the fundus images and SLO images in our work.

Piecewise linear mapping function

This method [32] rather than using one global mapping function to register the whole images, uses a number of local mapping functions, each tuned to map well in local neighbourhoods. Then by piecing the local mapping functions together, a global mapping is obtained. This is an interpolation approach: the surfaces f and g pass exactly through the 3-D points (x_i, y_i, X_i) and (x_i, y_i, Y_i), respectively, and determine the surface values at non-control points by interpolation of surface values at nearby control points.
The procedure can be divided in three parts: triangulation, linear interpolation and extrapolation. Using control points in the images, each image is divided into triangular regions, Figure 4.9 (a): a triangle is obtained such that any point in a triangle is closer to the three vertices that make the triangle than to vertices of any other triangles. The triangulation is determined in one of the images; in the other image is automatically obtained from the correspondence between control points.
For each pair of corresponding triangles in the images, the mapping functions that will register the two triangles are determined in the 'linear interpolation' phase. The problem of finding the linear mapping functions that will overlay the triangles can be stated in the form that: given 3-D points determine parameters of plane X = f(x,y) that will pass through these points. The equation of a plane passing through three points $(x_1, y_1, X_1),\ (x_2, y_2, X_2),$ and (x_3, y_3, X_3) is given by,

$$Ax + By + CX + D = 0 \tag{4.28}$$

where

$$A = \begin{vmatrix} y_1 & X_1 & 1 \\ y_2 & X_2 & 1 \\ y_3 & X_3 & 1 \end{vmatrix}; B = -\begin{vmatrix} x_1 & X_1 & 1 \\ x_2 & X_2 & 1 \\ x_3 & X_3 & 1 \end{vmatrix}; C = \begin{vmatrix} x_1 & y_1 & 1 \\ x_2 & y_2 & 1 \\ x_3 & y_3 & 1 \end{vmatrix}; D = -\begin{vmatrix} x_1 & y_1 & X_1 \\ x_2 & y_2 & X_2 \\ x_3 & y_3 & X_3 \end{vmatrix};$$

Given the coordinates of a point in the reference image (x,y), we can determine the X-component coordinate of the same point in the moving image using the linear mapping function of 4.28. The Y-component of the point is determined similarly.
The last step is the determination of the functions for mapping the points outside the convex hulls by extending the boundary triangle planes, Figure 4.9 (b).

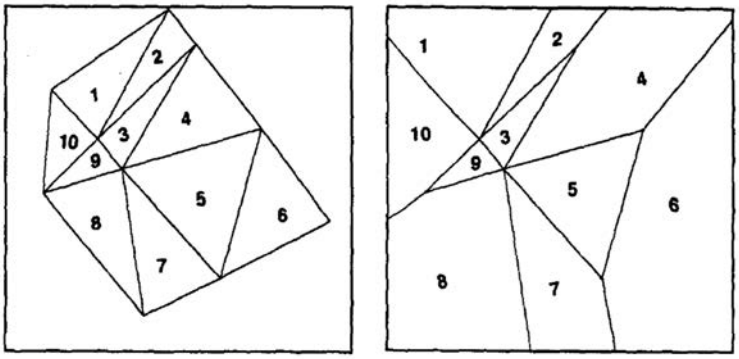

Figure 4.9: (a) Triangulation of a set of control points in an image. (b) Extension of a triangle planes to cover points between the convex hull and image borders.

Local weighted mean

The idea lying behind this method [33] is that if a point (x, y) in the reference image is near a control point i, then we expect that the corresponding point in the moving image would be also near control point i. This leads to determine the X value of a point (x, y) by the X values of the nearby control points, with appropriate weights. The registration transformation function is so defined by

$$f(x,y) = \frac{\sum_{i=1}^{N} W_i(x,y) X_i}{\sum_{i=1}^{N} W_i(x,y)} \tag{4.29}$$

where, the weight function, to make the method local is so defined

$$\begin{cases} W_i(R) = 1 - 3R^2 + 2R^3 & 0 \leq R \leq 1 \\ W_i(R) = 0 & R > 1 \end{cases} \tag{4.30}$$

where $R = [(x - x_i)^2 + (y - y_i)^2]^{\frac{1}{2}}/R_n$ and R_n is the distance of point (x_i, y_i) from its $(n-1)$th nearest control points in the reference image.
Using the weight function 4.30 in the mapping function 4.29, define the X value at an arbitrary point (x, y) by the weighted sum of polynomials having a nonzero weight over that point

$$f(x,y) = \frac{\sum_{i=1}^{N} X\{[(x - x_i)^2 + (y - y_i)^2]^{\frac{1}{2}}/R_n\} P_i(x,y)}{\sum_{i=1}^{N} W\{[(x - x_i)^2 + (y - y_i)^2]^{\frac{1}{2}}/R_n\}} \tag{4.31}$$

where $P_i(x, y)$ is the polynomial passing through measurement (x_i, y_i, X_i) and $n - 1$ other measurements nearest to it.
If the distribution of the control points is not uniform, so that no control points fall in a large area of the image, then it could happen that none of the fitted polynomials will pass over that area, leaving a hole in the image. In this case, new control points should be selected.

4.4 Quantitative evaluation measurements

One of the critical tasks of selecting the right image segmentation approaches for different medical image analysis tasks is to determine the accuracy of the algorithms. The accuracy is required in order to prove the improvement of the new algorithm compared with the current algorithms.
Many measurements have been presented to evaluate the segmentation approaches' performance. The most common measurements include similarity measurements and distance measurements. The similarity measurements compare the consistency between the ground truth and the automated segmentation. The distance index measures the difference distances between the contour of the ground truth and the automated segmentation. These measurements are explained in more detail in the following sub-sections.

4.4.1 Similarity measurements

Similarity coefficients measures how well two segmentation overlap. Two similarity coefficients are commonly used to measure the fraction of spatial overlap between two binary images, a ground truth and a proposed automated segmentation method.
The *Sørensen–Dice* index is a measurement of spatial overlap used widely for comparing segmentation results, with a value ranging from 0 to 1. The Dice coefficient can be defined as two times the area of the intersection between two segmentations divided by the sum of the area of the two segmentations. Given two sets, X and Y, is defined as

$$Dice(X,Y) = \frac{2 \mid X \cap Y \mid}{\mid X \mid + \mid Y \mid}, \tag{4.32}$$

where $\mid X \mid$ and $\mid Y \mid$ are the cardinality of the two sets. Using the definition of true positive (TP), false positive (FP), and false negative (FN), Figure 4.10, it can be written as

$$Dice(X,Y) = \frac{2TP}{2TP + FP + FN} \tag{4.33}$$

The *Jaccard* coefficient measures similarity between finite sample sets, and is defined as the size of the intersection divided by the size of the union of the sample sets:

$$Jaccard(X,Y) = \frac{\mid X \cap Y \mid}{\mid X \cup Y \mid} \tag{4.34}$$

The Jaccard coefficient can also be expressed in terms of true positives (TP), false positives (FP) and false negatives (FN) as:

$$Jaccard(X,Y) = \frac{TP}{TP + FP + FN} \tag{4.35}$$

The Dice index is related to the Jaccard index according to:

$$Dice(X,Y) = \frac{2 * Jaccard(X,Y)}{1 + Jaccard(X,Y)} \tag{4.36}$$

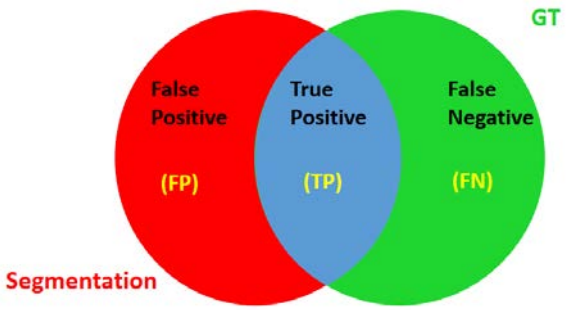

Figure 4.10: TP: pixels correctly segmented as foreground. FP: pixels falsely segmented as foreground. TN: pixels correctly detected as background. FN: pixels falsely detected as background.

4.4.2 Distance measurement

The above mentioned similarity coefficients do not demonstrate the dissimilarity between the boundaries of the ground truth and the automated image explicitly, which may be more interesting than the overlap area in many applications. Measuring the distance between two contours quantifies the amount of mismatch between two sets of points. We employed as measurement the average distance computed between the two contours.
In particular, let the ground truth GT contour discretized in n points $(g_1, g_2, \ldots, g_n)$ and the algorithm A resulting contour $(a_1, a_2, \ldots, a_n)$, Figure 4.11.
For each point g_i, $i = 1, \ldots n$ is calculated the Euclidean distance between the point and the closest point belonging to A to the point itself in the radial direction,

$$d(g_i, A) = min_j \|a_j - g_i\|, \qquad j = 1, \ldots, n. \tag{4.37}$$

The final index, Cd, is the distance averaged over all contour points

$$Cd(GT, A) = \frac{1}{n} \sum_{i=1}^{n} d(g_i, A) \tag{4.38}$$

A high value of 4.38 implies that the two contours do not match closely.

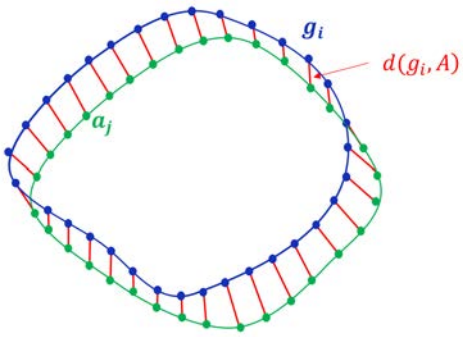

Figure 4.11: The green contour represents the GT, the blue one is the algorithm result. In red the distances 4.37.

4.5 Chapter summary

In this Chapter the theoretical tools used to understand our proposed methods are provided, dividing the same in three categories and for each tools the section in which is used has been reported.
In the next Chapter we will illustrate in details the proposed methods for OD detection in SLO images.

Chapter 5

Proposed methods

5.1 About this chapter

We developed two methods for automatic locating the optic disc in scanning laser ophthalmoscope images.
These methods have a first common part in which the OD is located, while they differ in the segmentation phase. To locate the OD they take advantage of the following observations on the OD's appearance in SLO images, Figure 5.1:

1. The OD is usually dark but it might have a lighter spot inside.
2. The contrast between vessels and OD is usually low.
3. The contrast between OD and background is usually high.
4. The shape is approximately elliptical.

Figure 5.1: An example of SLO image.

The two methods will be illustrated in details in the following two Sections, while the results of the methods are provided in the next Chapter.

5.2 Elliptical OD rim approximation via morphological operations

The first method has been developed at the beginning of the research study on a dataset consisting of 20 images.
Basically the algorithm, after defining a region of interest, seeks inside this ROI the OD segmentation. During the process, several OD segmentation candidates are generated through a sequence of morphological operations and the final segmentation is the ellipse that fits the best segmentation among all of them.
The algorithm can be divided in six main steps as in Figure 5.2:

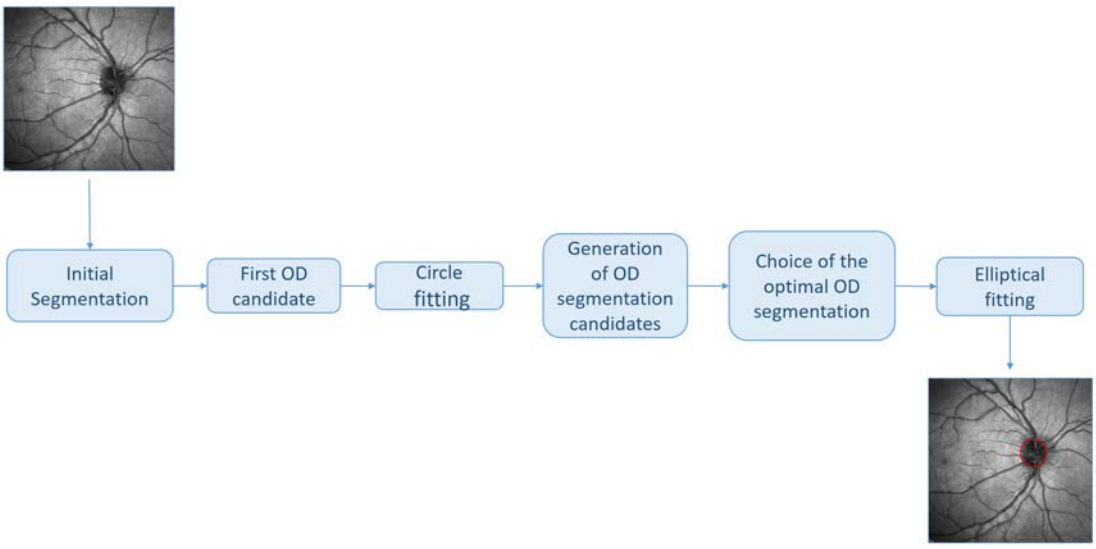

Figure 5.2: Pipeline of the algorithm

5.2.1 Initial segmentation

In the first step the algorithm performs an initial segmentation of optic disc along with the main vessels. A way to achieve this result is to iteratively run an adaptive thresholding. The thresholding is computed by setting the ratio

$$R = \frac{number\ of\ foreground\ pixels}{number\ of\ background\ pixels} \tag{5.1}$$

to 0.15. This number was set experimentally.
The adaptive thresholding is computed with the MATLAB built-in function *adaptthresh*; it takes as input the image to be thresholded and the *sensitivity* parameter, that is a scalar in the range [0,1] that indicates sensitivity towards thresholding more pixels as foreground.
We used the bisection method, explained in Section 4.2.1, to set, for each image, the parameter *sensitivity* in order to reach the condition $R = 0.15$.
In particular, looking at the pseudocode 4.2.1, the interval $[l, r]$ is equal to

$[0, 1]$. At each iteration, the idea is looking for greater value of sensitivity if the percentage of pixel thresholded on the total pixels of the image is greater than the target value (0.15), lower value of sensitivity otherwise. The exit condition for the while loop is $R = 0.15$. A result of the initial segmentation is shown in Figure 5.3.

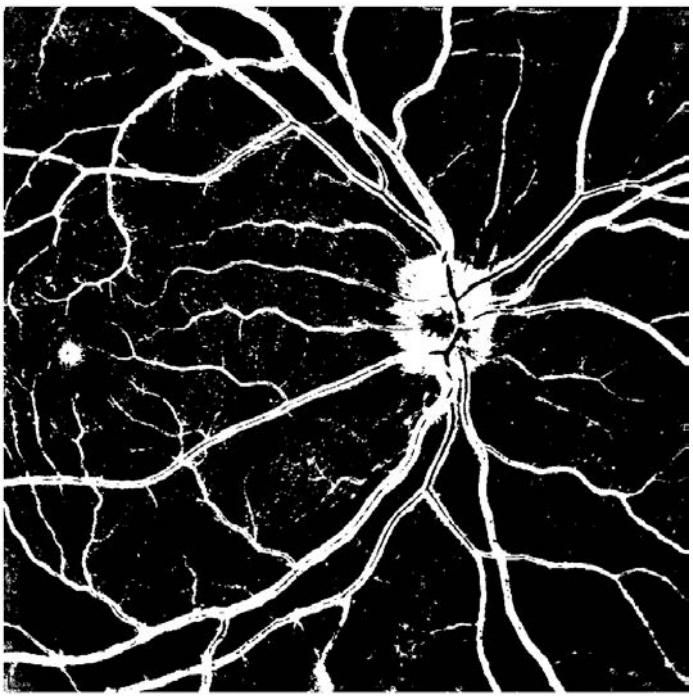

Figure 5.3: Result of the initial segmentation step in an image of the dataset.

5.2.2 First OD candidate

In the second step we generate a first OD candidate through a sequence of morphological operations; the idea is to separate the optic disc from the vessels and keep only the OD.
From the initial segmented image, a preliminary opening operation is carried out with the aim of dividing the OD from vessels. In this case the structuring element has a disc shape of radius 15. Then, the largest connected component in terms of number of pixels is kept and a closing operation is performed to not lose information.
At this point the binary image is refilled through a closing operation with a disc structuring element of radius equal to the estimated radius of the segmentation itself. The resulting image is considered as a first OD segmentation.
At the end the centre of gravity of the result of this stage is calculated and given as input to the circle fitting step. Despite this procedure is similar to the one proposed in [17], it was developed independently.
It is not required high precision at this stage, since the goal is to find a region in which the optic disc is located. The entire procedure is illustrated in Figure 5.4.

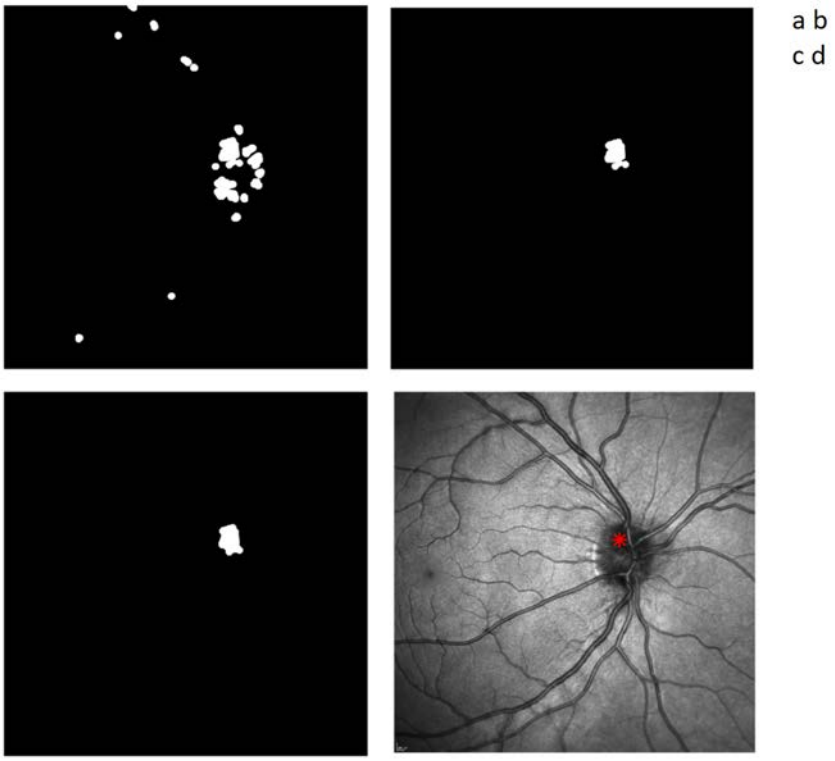

Figure 5.4: First OD candidate: (a) Opening to split OD and main vessels. (b) Largest connected component. (c) First OD segmentation. (d) OD centre coordinates calculated as the centre of gravity of (c).

5.2.3 Circle fitting

Looking at this kind of images we can recognize the optic disc as the structure with both high radial (circular) symmetry and high contrast between the inner and outer region.
For this reason, a first form of contour is given by fitting the circle that maximize the contrast between the inner and outer region.
It has been used circle fit already implemented in the software VAMPIRE 3.1.2.
The optimal circle is found by initializing circles in the ROI, detected at the previous step, running the deterministic Nelder-Mead optimizer, see Section 4.2.2. The initial possible values for the radius are [100, 120, 140, 160], while the initial OD centre coordinates have been calculated at the end of first OD candidate step. The final result is the circle that has minimum value of the cost function. The steps for building the cost function [26] are listed below:

- Sample the contour at N discrete points
- for each point $\mathbf{p}(i) = (x_i, y_i)$, compute the unit vector $\mathbf{n}(i)$ perpendicular to the contour
- sample S equally spaced internal points $C_{in}(i,k) = \mathbf{p}(i) - k\alpha\mathbf{n}(i),\ k = 1, \ldots, S$

– sample S equally spaced external points $C_{out}(i,k) = \mathbf{p}(i) - k\beta\mathbf{n}(i),\ k = 1,\ldots,S$

The cost function is defined as,

$$F(C) = \sum_{i=1}^{N}\sum_{k=1}^{S} w(k)min\{I[C_{in}(i,k)] - I[C_{out}(i,k)], D\} \tag{5.2}$$

where $w(k)$ are weights that are maximal for small k, and D is a constant value representing a reasonable value for the difference between inner and outer intensity. In our method the parameters are:
$N = 30,\ S = 8,\ D = 50,\ \alpha = 0.8R/S\ \beta = 0.5R/S.$

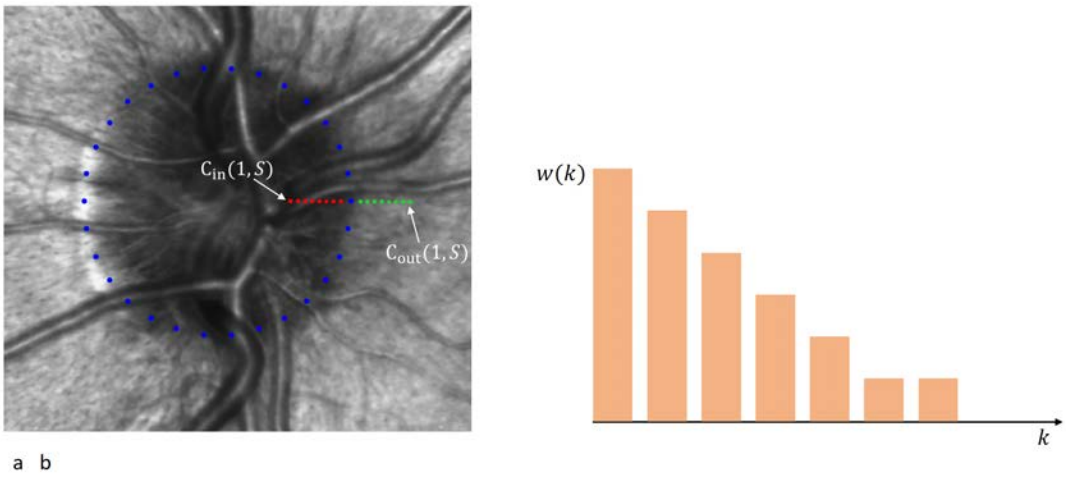

Figure 5.5: (a) Optimal sampled circle (blue dots), set of inner points (red dots) and set of outer points (green dots). (b) Weights that multiplies the differences between the two sets into the cost function.

For a better comprehension of the cost function, refer to Figure 5.5.
To the optimal circle was assigned a score: let the local contrast (LC) for each sampled point $\mathbf{p}(i)$ defined as,

$$LC(i) = \sum_{k=1}^{S} w(k)min\{I[C_{in}(i,k)] - I[C_{out}(i,k)], D\},$$

that indicates the weighted sum between the set of inner points along the perpendicular to the circle and the set of outer points.
Define a *red_point* as a point of the sampled circle in which the LC computed for that point is lower than a certain threshold h ($h = 60$). We can define e, a scalar proportional to the number of red points on the total number of sampled points (N), as

$$e = (\frac{\#red\_points}{N})\rho,$$

$$red\_points := \mathbf{p}(i)\ s.t.\ LC(i) < h,\ i = 1,\ldots,N.$$

The coefficient of proportionality is ρ and is set to 0.3. The reliability coefficient α for the optimal circle is

$$\alpha = (1 - e) \tag{5.3}$$

is a measure of how many points in the circle are considered as a edge points due to the contrast in the radial direction.

5.2.4 Generation of OD segmentation candidates

In the 4th step the algorithm generates several OD segmentation candidates to choose among, Figure 5.6. Starting from the result obtained by the initial segmentation, the generation of the candidates is performed by subsequent and more aggressive closing operation. This means that the structuring element dimension increases at each candidate.
In order to limited the computation and to avoid including the vessels into the segmentation, the operations are conducted only inside the mask defined by the optimal circle.

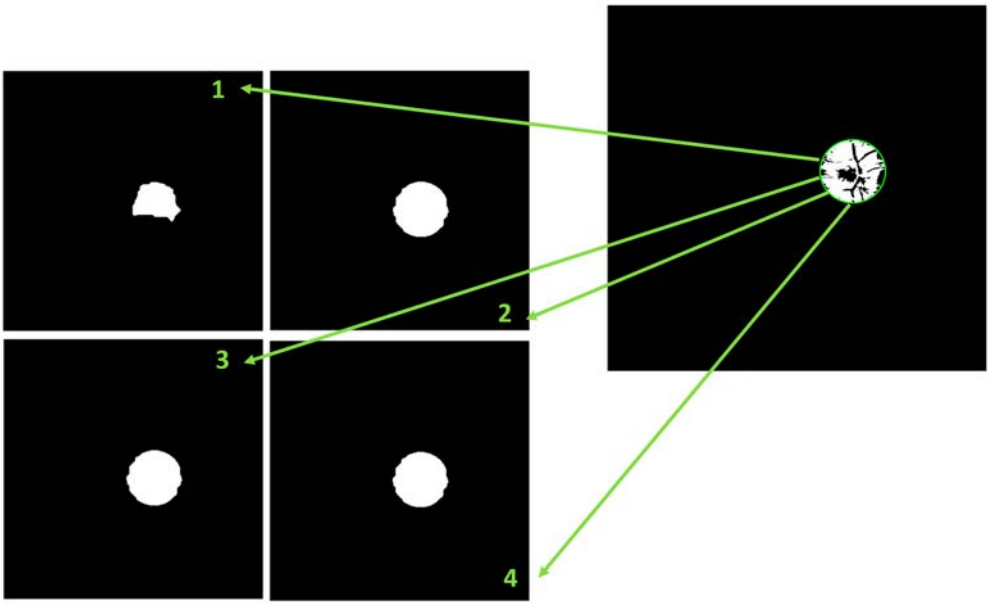

Figure 5.6: Generation of several OD candidates starting from the segmented image.

5.2.5 Choice of optimal OD segmentation

Once we generate the candidates we have to choose one as the final segmentation, so we need a criterion.
In the dataset we observed that the optimal circle area (OCA) is usually equal or greater than the OD area. So, intuitively, the best OD candidate is the one whose area is close to the OCA. But, since the circle is just an approximation of the OD, this criterion is not enough. In fact, the circle will fit well some

part of OD contour and badly other parts; this information is incorporate in the reliability coefficient for the optimal circle, α (5.3).
The final criterion is to select the segmentation that is close enough to both the optimal circle and to a percentage of the optimal circle, given by α, i.e. α(OCA). In formulas, defining

$$C1 = \frac{OCA - A_c}{OCA} \tag{5.4}$$

and

$$C2 = \frac{A_c - \alpha(OCA)}{A_c}, \tag{5.5}$$

where A_c is the area of the segmentation candidate.
Choose the segmentation that

$$minimizing\ C = C1^2 + C2^2 \tag{5.6}$$

In Figure 5.7 an example of final segmentation, chosen according the above criterion.

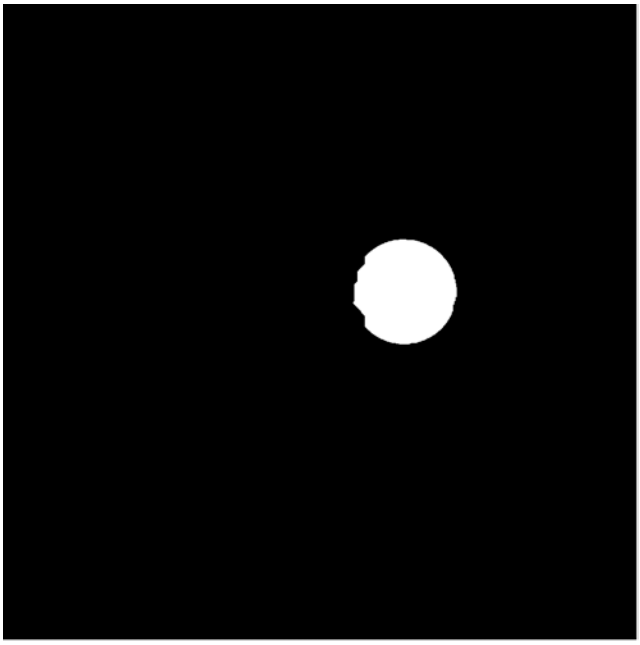

Figure 5.7: OD segmentation candidate chosen according the criterion 5.6.

5.2.6 Elliptical fitting

At the end a fit ellipse is performed on the final segmentation as described in Section 4.2.3.
In detail:

1. after choosing the OD segmentation (binary image), Figure 5.7
2. calculate the OD contour as the perimeter of the segmentation

3. sample the contour
4. run the ellipse fitting function on a set of sampled contour points
5. the final segmentation is the ellipse that best fits the binary image

A result is shown in Figure 5.8, the white contour is the segmentation found, while the red one is the result of fit ellipse.

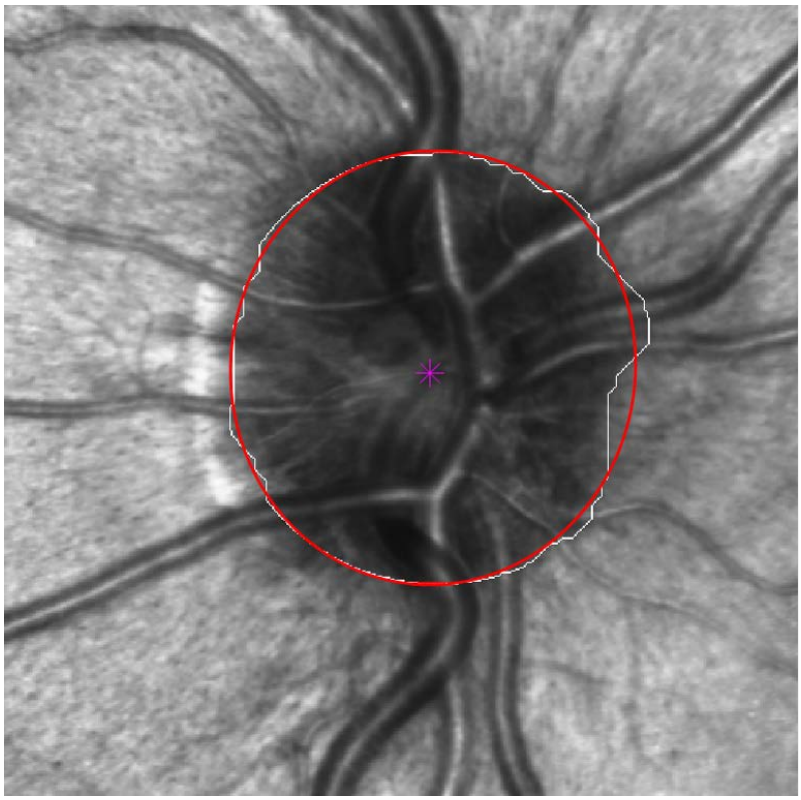

Figure 5.8: Final result. The white contour is the best OD segmentation choose according the criterion 5.6. The red contour is the fit ellipse result.

5.3 Hand-crafted features for OD contour points selection

After the formulation of the first method, our studies focused on the need of either obtain more precise free-form contour and faster performance of the algorithm.
To achieve the above mentioned purposes, a ultimate method has been developed for the automatic location and segmentation of the optic disc in SLO images.
Initially, the algorithm locates a ROI containing the OD, as processed in the first steps of the previous algorithm. Then the algorithm extracts hand-crafted features within the ROI, along the OD contour. The final contour is identified

by an optimization in the space of the possible shapes of a deformable contour. Referring to Figure 5.9, we can see that the first three steps of the first algorithm, upper windows, are gathered in a single block that is the first step of the new algorithm.
The method is divided in five steps as described below.

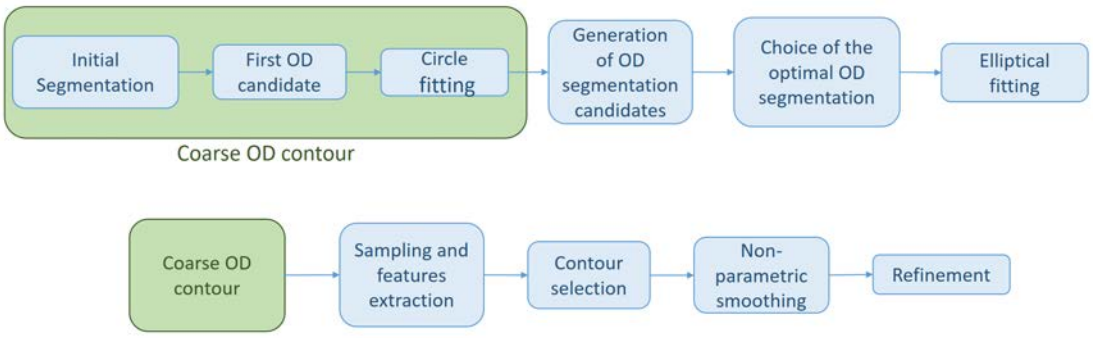

Figure 5.9: Scheme of the first algorithm, upper window. Pipeline of the second method, bottom window.

5.3.1 Coarse OD contour

The first step includes the initial segmentation, first OD candidate and circle fitting. The initial segmentation and first OD candidate steps are the same defined in the previous Section. While we have slightly modified the cost function in the circle fitting step by adding a regularization term related to the overall intensity level of the circle contour. It is possible to vary the strength of this term by setting the parameter α. Giving name $F_c(C)$ to the cost function defined in 5.2, the cost function with regularization term is :

$$F(C) = F_C(C) + \alpha I_m, \tag{5.7}$$

where F(C) is the contrast between the inner and the outer region, I_m is the mean intensity along the circle. The α parameter takes value in the range $[0,\ 1]$, where 0 leads to prefer darker OD contours, while 1 leads to brighter contours.

5.3.2 Sampling and feature extraction

Here, our goal is to discriminate OD's edge points in the ROI. Before going through the details of this stage, observing the images in the dataset, we can state that:

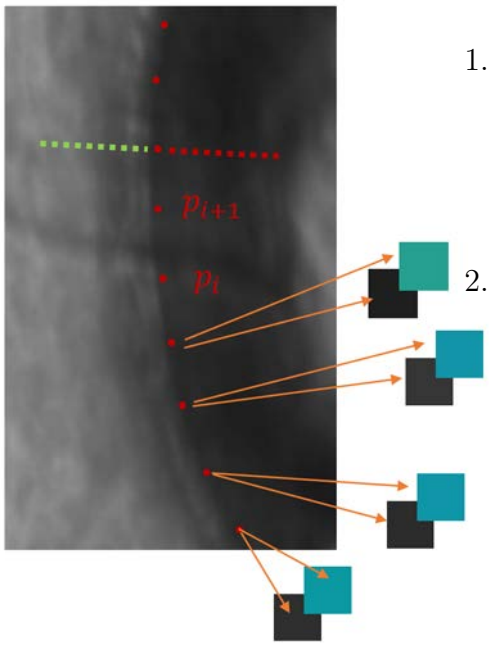

1. Points belonging to the same edge share some features, such as
   (a) intensity (i)
   (b) contrast (c)
2. The contrast computed over the OD's edge points is usually high.
   In the side figure, a magnification of the contour. Here, for each point $\mathbf{p_i}$, the overlapped square represent the intensity, and the bottom square the contrast.

It is possible to generalize (1.) to m features

$$\mathbf{p_i} = \begin{pmatrix} i \\ c \end{pmatrix} \quad \rightarrow \quad \mathbf{p_i} = \begin{pmatrix} f_i^{(1)} \\ f_i^{(2)} \\ \vdots \\ f_i^{(m)} \end{pmatrix} \tag{5.8}$$

such that a point $\mathbf{p_i}$ is a vector in $\mathbf{R}^m$ identified by its features. At this stage we suppose to be close to the ideal contour, hence we sample around the contour and over these sampled positions in the image we extract several features. Observing Figure 5.10 (a), the points are sampled as following:

- N samples along the contour (blue dots)
- n samples in radial direction at frequency f_c :
  - $(n-1)/2$ samples inside the contour (red dots)
  - $(n-1)/2$ samples outside the contour (green dots)

At the end we got nxN pixels sampled matrix (PSM), Figure 5.10 (b): the pixels coordinates in the original image are stored in a $nxNx2$ matrix.
Basically, with "features extraction" we mean to filter the sampled image (PSM) to obtain feature maps.
Feature maps computed are:

1. *Contrast*: radial contrast between inner/outer region computed on OD contour points, should be high in radial direction and homogeneous in the normal direction.
   A common way to extract edges is to filter an image with a derivative of Gaussian filter. The Gaussian filter is defined as,

$$h_\sigma(u,v) = \frac{1}{2\pi\sigma^2} e^{-\frac{u^2+v^2}{2\sigma^2}}, \tag{5.9}$$

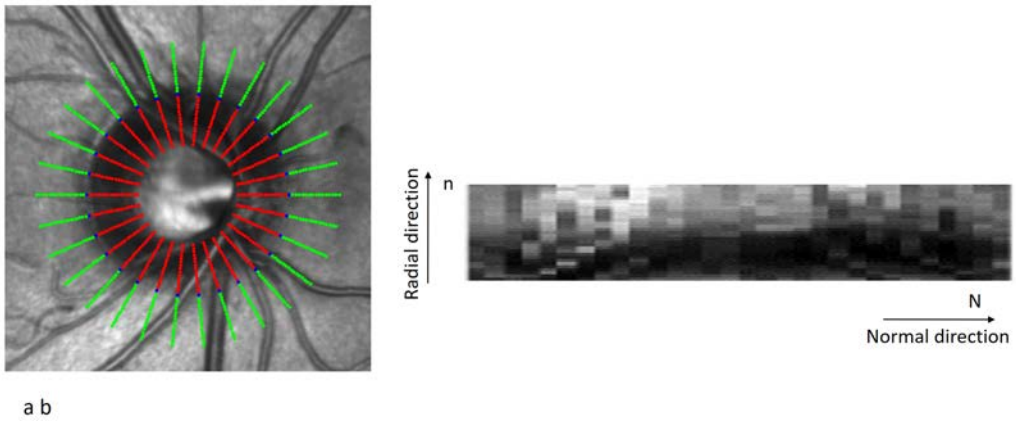

Figure 5.10: Sampling grid of the contour (a). Blue dots are the sampled contour, red dots inner points, green dots outer points. PSM matrix (b)

so the derivative of Gaussian along x direction is

$$\frac{\partial}{\partial x} h_\sigma(u, v). \tag{5.10}$$

In Figure 5.11 are reported a Gaussian filter and a derivative of Gaussian. We use a 1-D derivative of Gaussian filter, Figure 5.12, in the radial

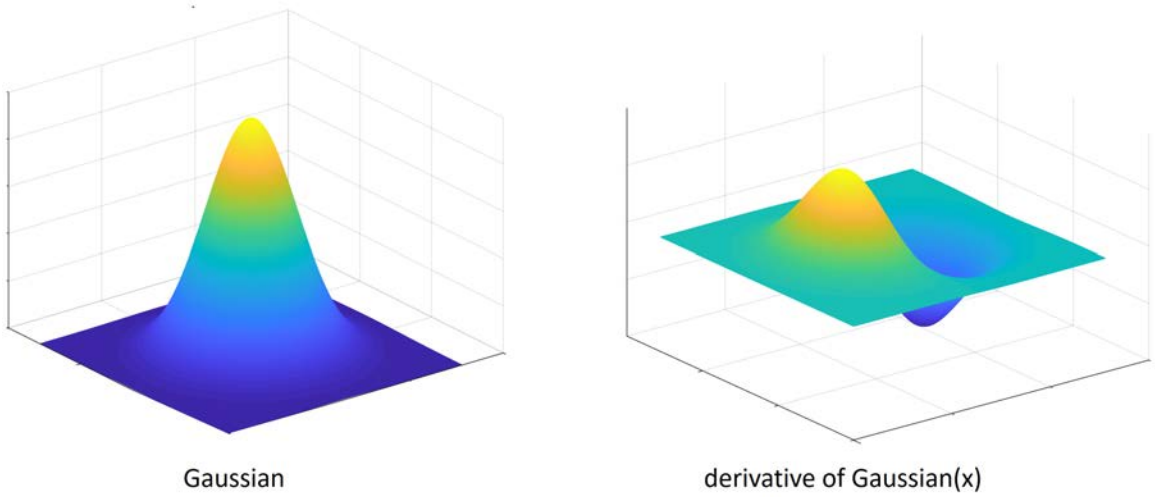

Figure 5.11: Gaussian filter on the left and derivative of Gaussian filter on the right side.

direction of the contour to obtain the 'Contrast' feature map. The filter size is [30 1] and $\sigma = 3$.

2. *Median filtered image*: median filter applied along the normal direction, in order to try to reduce the vessels information. The median filter is a sliding-window spatial filter, it replaces the center value in the window with the median of all the pixel values in the window. The median is calculated by first sorting all the pixel values from the surrounding

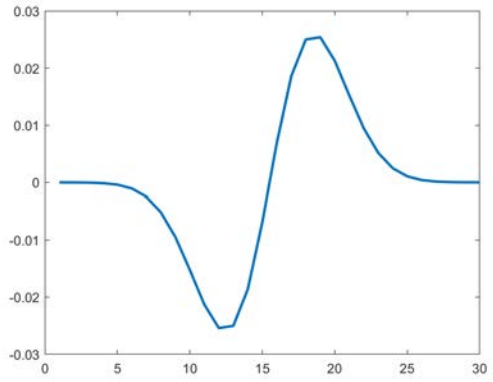

Figure 5.12: 1-D derivative of Gaussian filter.

neighbourhood into numerical order and then replacing the pixel being considered with the middle pixel value. If the neighbourhood under consideration contains an even number of pixels, the average of the two middle pixel values is used.
In our case the window size to filter the PSM is $[1\ mspan * 2 + 1]$, where $mspan$ is related to the number of samples N according the relation $mspan = round(\frac{N}{30})$.

3. *Radius*: close points along the contour share the same distance from the centre.
The 'radius' map has got by the computation, for each point in the grid, of the Euclidean distance from the OD centre.

4. *Contrast on median filtered image*: contrast (1.) computed on feature map 2.

The feature maps, Figure 5.13, are stacked in a 3-d array of size $nxNx4$.

5.3.3 Contour selection

Ideally, the goal of this step is finding the best set of points (4-d) defining a contour among all the possible sets. For this scope we built a cost function that assigns a cost to a set of points. The cost is given in order to penalize set of points in which the intra-variability of the features is high, and the overall contrast is low. In detail, for each point $\mathbf{p_k}$ the Euclidean distance between $\mathbf{p_k}$ and all the others points in the set is computed and then weighted by their relative position in X. The sum of all the distances is finally multiplied by the contrast feature of $\mathbf{p_k}$ itself. We select the optimal set of points $\{\mathbf{p_1}, \mathbf{p_2}, \cdots \mathbf{p_N}\}$ such that

$$I^* = \underset{I=\{\mathbf{p_1},\mathbf{p_2},\cdots\mathbf{p_N}\}}{\operatorname{argmin}} \sum_{k=1}^{N} c_k \sum_{\forall j:\mathbf{p_j}\in I} w(j-k)d(\mathbf{p_k},\mathbf{p_j}), \tag{5.11}$$

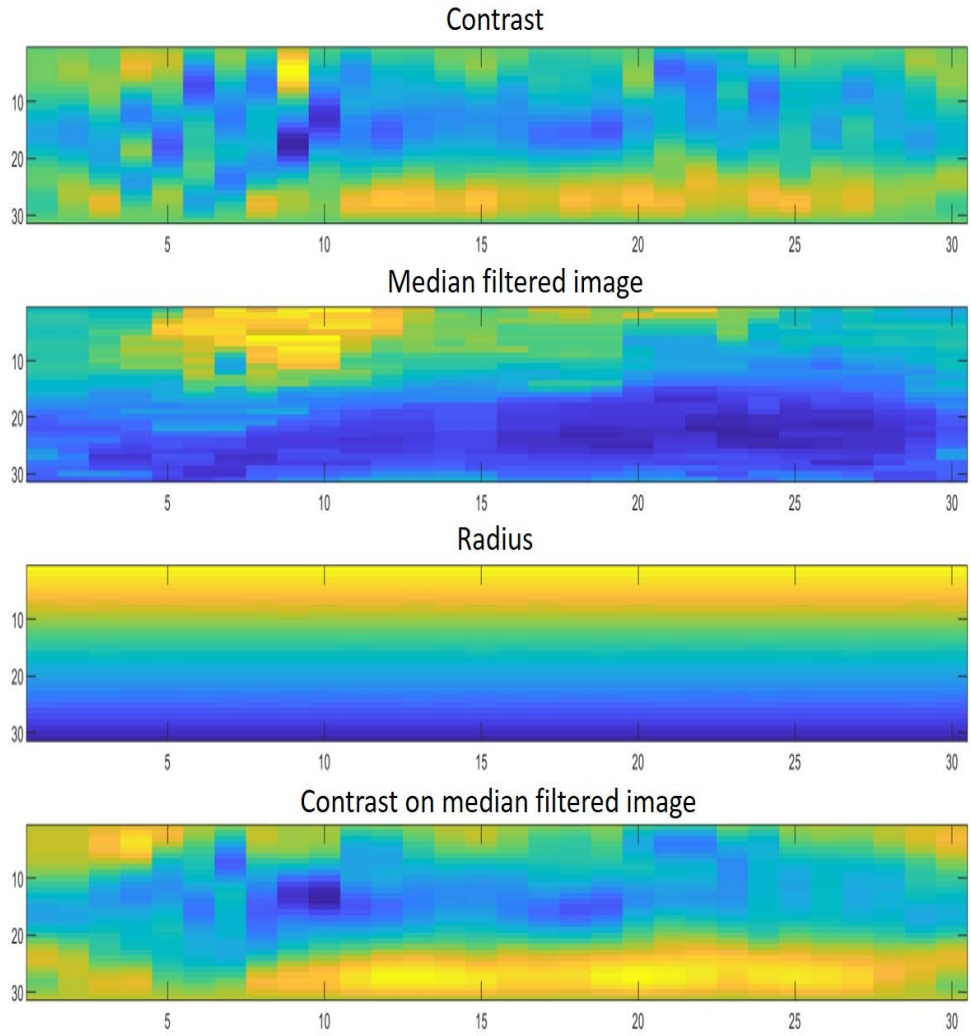

Figure 5.13: Hand-crafted feature maps

where:
I^* : optimal set
I : set of edge candidates points
N : number of columns of the sampling grid
$w(t)$: spatial weight function
$d(\mathbf{p_i}, \mathbf{p_j})$: distance function
c_k : contrast features of $\mathbf{p_k}$.
The selection is operated trying to minimize the cost function through an iterative procedure leading to a suboptimal solution. The routine starts choosing an initial point from which, step by step, all the others points are selected; at each iteration the point that minimize the cost is added to the final sequence. The initial point is drawn according to the following cost function:

$$score(\mathbf{p_k}) = \sum_{\forall j:\mathbf{p_j}\in I} w(j-k)d(\mathbf{p_k}, \mathbf{p_j}). \tag{5.12}$$

In other words, the more similar the point is from the rest of the contour the

lower is its score.

5.3.4 Non-parametric smoothing

To obtain regular contour we perform a non-parametric smoothing, Section 4.3.3, on the one obtained at the previous step using, as penalization, the score computed on the contour itself. We implemented the formula 4.27, where:

- **y**: signal to be smoothed, defined as the distance between each contour point and the OD centre
- **B**: diagonal matrix where b_{ii} is the score of $\mathbf{p_i}$, as in 5.12
- **F**: Toeplitz matrix 4.26, that penalizes the second-differences (m=2)

The balance between smoothing and fitting is settled by the parameter *gamma*: smaller gamma corresponds to higher fitting, while larger gamma corresponds to stronger smoothing. In Figure 5.14 are shown results obtained with different values for gamma. Typical values are in the range $[10^{-5} \div 10^{5}]$, in which 10^{-5} means no regularization and 10^{5} means maximum regularization. We fixed $\gamma = 100$, but it is a user parameter an it can be tuned. The smoothing was performed on a virtual grid with number of samples N equal to 150.

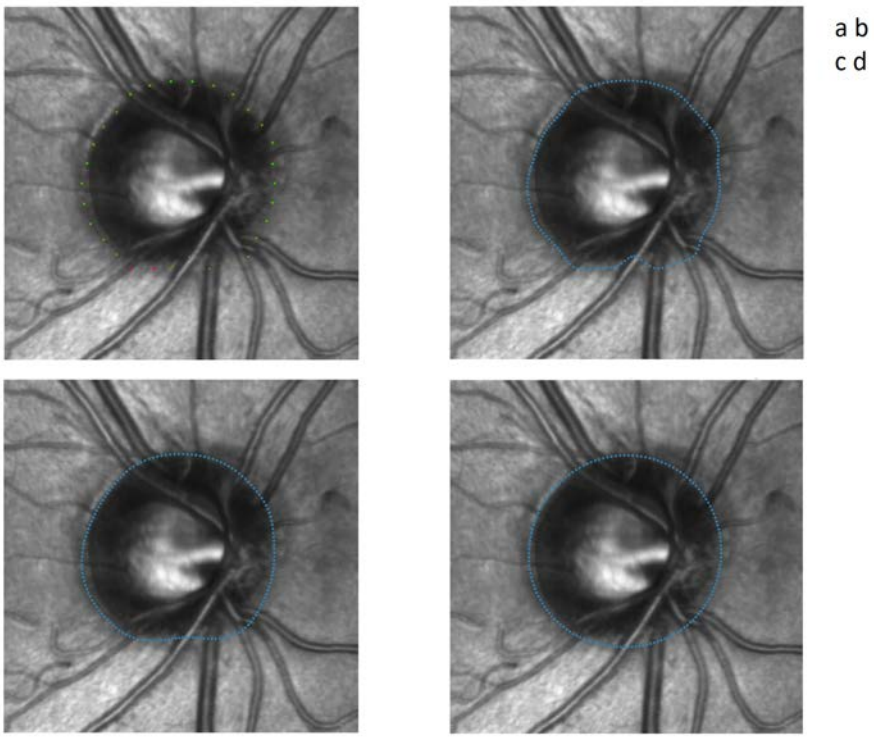

Figure 5.14: Results obtained for different values of gamma.
Result of contour selection at first iteration (a). Non-parametric smoothing with $\gamma = 0.001$ (b), $\gamma = 100$ (c), $\gamma = 10000$ (d).

5.3.5 Refinement

The contour resulting from step 4 is then refined by repeating steps 2, 3, 4. In the direction of getting more accurate information we increase both the number of samples along the contour and the sampling frequency along the radial direction (f_c). In Figure 5.15 some results are reported.

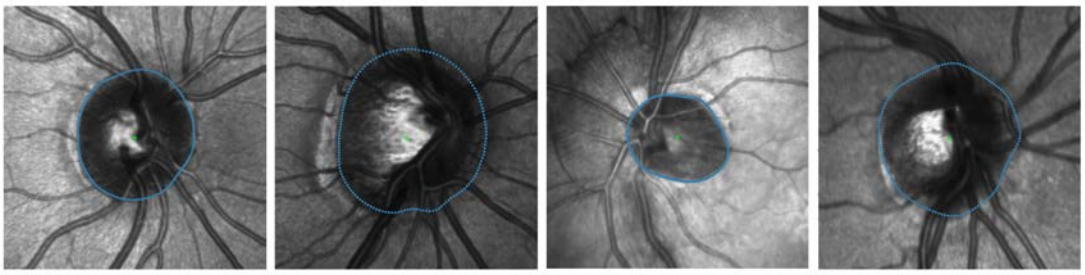

Figure 5.15: Results obtained in a sub-set of the images in the dataset.

5.4 Chapter summary

In this Chapter we presented two methods for OD localization in SLO images. These methods have a common detection phase, while differ in the segmentation step. The detection of the OD is achieved by searching in the image the largest connected component. After ROI identification, the first method, named '*Elliptical OD rim approximation via morphological operations*', segments the OD through a sequence of morphological operations. The second method, named '*Hand-crafted features for OD contour points selection*', selects the OD boundary via cost function minimization, based on features *ad hoc* computed within the ROI.
The quality of the results of the first and second methods will be evaluated in the next Chapter. The performances of the algorithms are compared with manually drawn annotations, as well as with the performance of a validate algorithm for the fundus images.

Chapter 6

Experimental results

6.1 About this chapter

This chapter presents the experimental tests and results of our methods.
First of all the method used for registering the fundus images will be illustrated. Then a characterization of the annotators will be conducted, with a brief discussion on the annotations of the peripapillary atrhopy (PPA) contour. At the end we make comparisons among the automatic and manual procedures. The performance of the proposed methods will be compared with respect to the reference standards, as well as the performance of the VAMPIRE algorithm with respect to the fundus images.

6.2 Multi-modal retinal image registration

Our goal is to find a method to register the fundus camera images and SLO images, so as discussed in Section 4.3.4, we are dealing with a multi-modal intra-patient image registration.
Multi-modal image registration is a primary step in integrating information stored in two or more images, which are captured using multiple imaging modalities. In medical applications is useful in monitoring the progression of diseases, quantifying the effectiveness of a treatment, surgery planning.
Multi-modal registration algorithms focus on finding correspondence between images generated using various modalities. For this reason comparing to mono-modal registration is more challenging due to the high variability of tissue appearance under different modalities, as well as the different sizes and resolutions [34].
The existing approaches for retinal imaging registration are usually based on pixels intensity or feature extraction of anatomical structures that correspond in the two images [35]. Despite all the efforts in studying the problem of registration there is no unique technique that works in all circumstances.
In our case we set up a semi-automatic procedure, Figure 6.1, to register the fundus camera images over the SLO images.

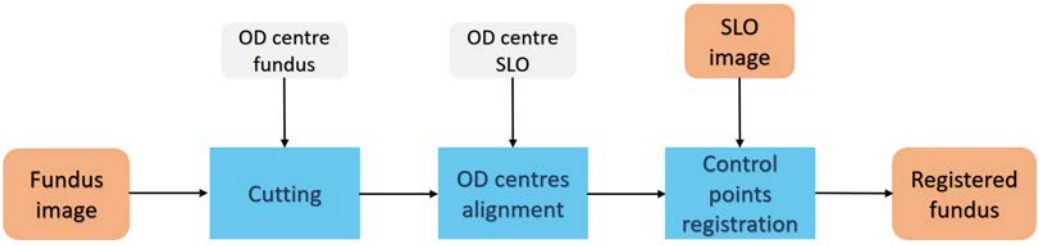

Figure 6.1: Sketch of the procedure for the registration.

Since the fundus image is larger than the corresponding SLO, the first step is cutting in the fundus image a ROI of the same size of the SLO image (1536x1536) around the OD centre. For this operation, useful to reduce the computational complexity, we use as coordinates of the OD centre the values resulting from the VAMPIRE algorithm.
Then we align the two images such that the centre of the optic disc in the two images corresponds. To do that we apply a simple *translation* transform, Figure 6.2. The OD centre in the SLO images is manually selected for each image.

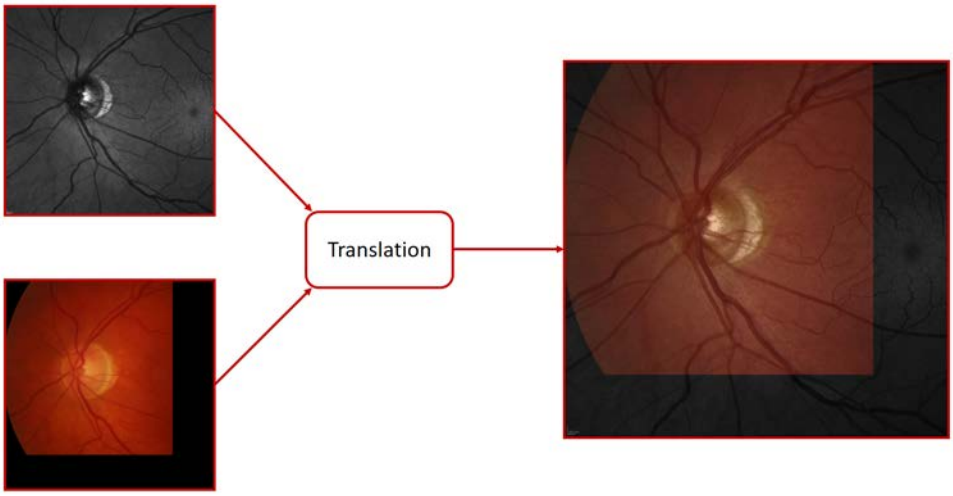

Figure 6.2: Shift of the fundus image such that the centre of the OD in the two images corresponds.

Basically after aligning the OD centres, we want to estimate the transformation that brings the two images to match.

We use the framework shown in Figure 6.3:

1. Find all valid pairs of control points in the moving (fundus) and fixed (SLO) images.

2. Infer a spatial transformation between moving and fixed control points.

3. Apply the spatial transformation to the new points in the image.

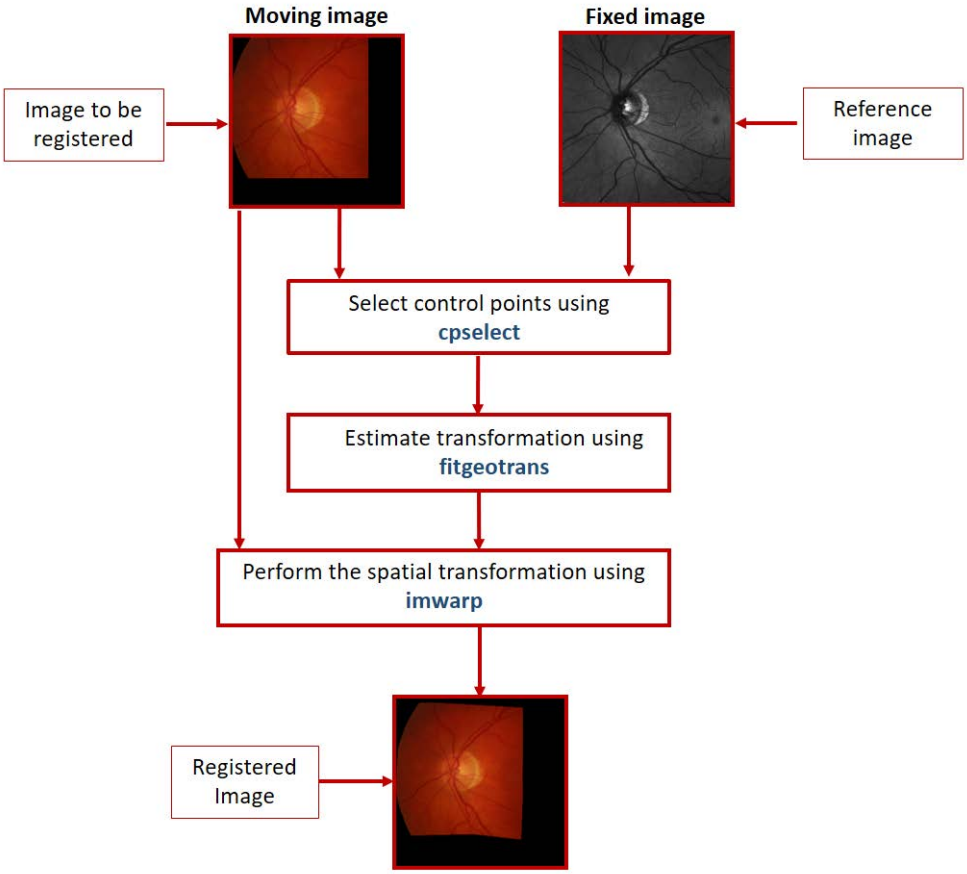

Figure 6.3: Framework used to register the fundus image over the SLO image [1]. In blue the functions of MATLAB that are used in each step.

In fact, image registration is usually carried out in two steps [36]. In the first, a number of control points are selected from the images. In the second, the position of corresponding control points in the images are used to determine a transformation function which maps the rest of the points in the images [37]. Control points are selected either manually or automatically. In our work we manually select the points using the '*Control Point Selection Tool*' of MATLAB, Figure 6.4. This tool is a user interface that enables you to select control points in two related images.

We manually select in the two images a set of corresponding points, trying to distribute them uniformly. Previous papers have shown that it is reasonable extract fixed landmarks likes blood vessel crossings and bifurcations from retinal images, as well as the fovea and points inside the OD [38]. An example of selected control points in the two images is provided in Figure 6.5.

After the points selection we want to estimate the transformation by taking the pairs of control points, moving and fixed, and using them to infer the geometric transformation. The hard part here is find the proper transformation that enables the images to overlap.

[1] https://uk.mathworks.com/help/images/control-point-registration.html

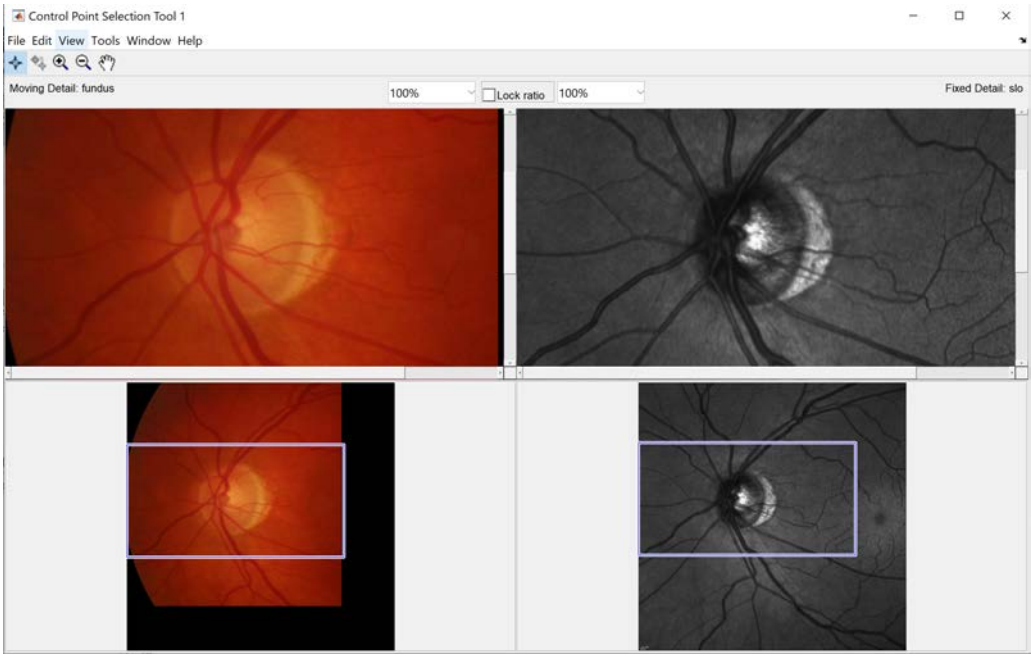

Figure 6.4: Control Point Selection Tool

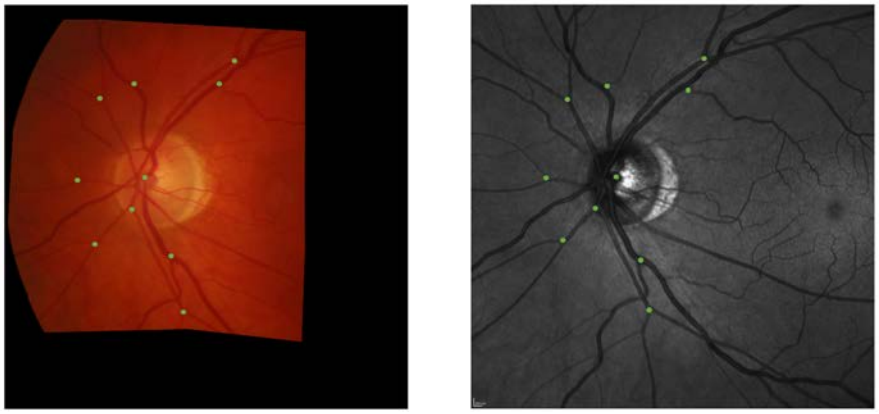

Figure 6.5: Example of set of control selected points in the moving (on the left) and fixed (on the right) image.

For each image we estimate two types of transformation: piecewise linear transformation ('pwl') and local weighted mean ('lwm'), described in Section 4.3.4. For each image both transformations were estimated and is chosen the one that gives the best overlap between the fixed and registered image. The amount of overlapping was assessed by visual inspection.

The accuracy of image registration was assessed by visual inspection for each image, showing the two images overlapped in a 'chessboard' visualization, as shown in Figure 6.6.

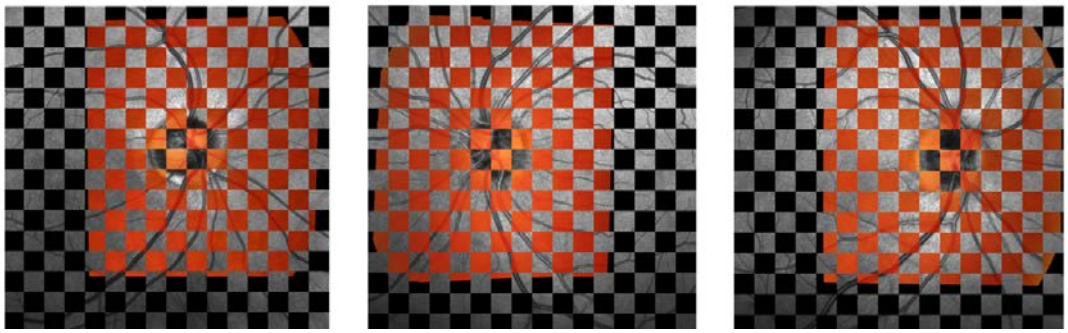

Figure 6.6: Examples of registered images overlapped to corresponding SLO images with chessboard visualization.

6.3 Inter- and intra-annotator reliability

In engineering, when we talk about reference standars for testing we refer in general to objective measurements; in medical image analysis, the references standards are instead built from statistical or explicit consensus among experts [11].
For example, in our case the ground truth are contours manually drawn.
Since it is known that the OD margin is complex and can be highly variable within individual eyes and between different eyes [10], there may be some disagreements among the annotators. Hence, before evaluating the performance of the algorithms against the annotators it is very interesting and useful assessing the inter- and intra-operator reliability.
We can refer to inter-operator reliability as the level of agreement among annotations, in our case manually drawn contours.
As said in Section 2.3 for testing our algorithm we have four annotators, A_1, A_2, A_3, A_4. Both inter- and intra-annotator variability will be tested with three measurements, Dice, Jaccard and the contour distance, reported in Section 4.4.
We made comparisons among all possible pairs of annotators: A_1/A_2, A_1/A_3, A_1/A_4, A_2/A_3, A_2/A_4, A_3/A_4.
In Table 6.1 are reported the comparisons with the three measurements, mean and standard deviation, in the SLO images; while in Table 6.2 are compared the annotations in fundus images.
Furthermore in Table 6.3 there is the mean agreement between the annotators in SLO and Fundus images; it gives as an idea of how much homogeneity or consensus there is in the ratings given by various annotators.

The annotators show an high inter-agreement, apart for some images in which the contour differ substantially. In Figure 6.7 we show the inter-agreement in SLO and fundus images, we can see that for some images the Dice coefficient is very low. We can note that for the SLO images the variability between the annotators is lower than in the fundus images.

Table 6.1: Table with the comparisons among annotators on SLO images.

	Dice *mean (std. dev.)*	*Jaccard* *mean (std. dev.)*	*Contour distance* *mean (std. dev.)*
A1/A2	0.92 (0.07)	0.86 (0.10)	16 (12.39)
A1/A3	0.91 (0.07)	0.85 (0.11)	20 (16.91)
A1/A4	0.94 (0.05)	0.89 (0.08)	15 (11.07)
A2/A3	0.94 (0.03)	0.90 (0.08)	13 (14.62)
A2/A4	0.94 (0.03)	0.90 (0.05)	12 (6.84)
A3/A4	0.94 (0.04)	0.89 (0.07)	13 (12.92)

Table 6.2: Table with the comparisons among annotators on fundus images.

	Dice *mean (std. dev.)*	*Jaccard* *mean (std. dev.)*	*Contour distance* *mean (std. dev.)*
A1/A2	0.92 (0.07)	0.85 (0.10)	23 (20.33)
A1/A3	0.87 (0.07)	0.78 (0.11)	30 (16.61)
A1/A4	0.92 (0.06)	0.85 (0.09)	21 (16.74)
A2/A3	0.93 (0.04)	0.87 (0.06)	18 (8.42)
A2/A4	0.95 (0.03)	0.91 (0.06)	13 (9.58)
A3/A4	0.93 (0.04)	0.87 (0.06)	18 (8.83)

Table 6.3: Mean Agreement among annotators.

	Dice *mean (std. dev.)*	*Jaccard* *mean (std. dev.)*	*Contour distance* *mean (std. dev.)*
SLO	0.93 (0.06)	0.88 (0.09)	15 (12.98)
FUNDUS	0.92 (0.06)	0.88 (0.09)	20 (14.96)

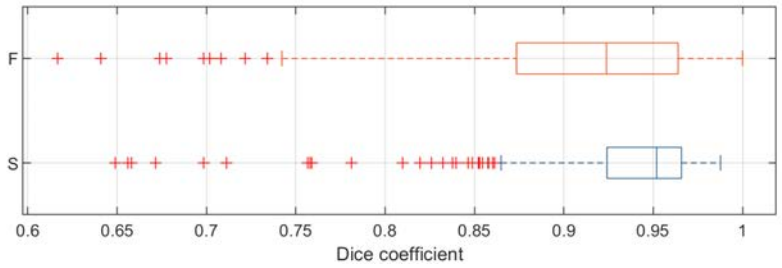

Figure 6.7: Orange box represents the inter-agreement between annotators on SLO images (S); blue box on fundus images (F). For each box the line inside represents the median value and the red '+' symbols represent the outliers.

On the other hand we have to take into account the variability over repeated judgments by the same expert (intra-observer variations).
We must keep in mind that annotating specific image elements, like in our case the OD contour, is a task that doctors do not normally perform in clinical practise. Hence, assess the intra-annotators reliability is a crucial part in the

validation process. In Table 6.4 there is the intra-operator reliability on SLO images, in Table 6.5 on fundus images. The intra-operator reliability was evaluated on a batch of 15 images.

Table 6.4: Intra-annotator variability in SLO images.

	Dice *mean (std. dev.)*	*Jaccard* *mean (std. dev.)*	*Contour distance* *mean (std. dev.)*
A1	0.94 (0.04)	0.90 (0.06)	11.70 (6.59)
A2	0.95 (0.03)	0.91 (0.05)	11.57 (7.27)
A3	0.95 (0.03)	0.91 (0.05)	11.35 (8.00)
A4	0.97 (0.02)	0.95 (0.03)	5.99 (3.32)

Table 6.5: Intra-annotator variability in fundus images[2].

	Dice *mean (std. dev.)*	*Jaccard* *mean (std. dev.)*	*Contour distance* *mean (std. dev.)*
A1	$\sim$	$\sim$	$\sim$
A2	0.96 (0.02)	0.93 (0.03)	10.50 (5.86)
A3	0.95 (0.03)	0.91 (0.05)	12.79 (7.03)
A4	0.97 (0.01)	0.95 (0.02)	6.34 (2.17)

All the annotators have a high intra-agreement with all the three indices. In particular the value of the point-to-point distance are very low, hence we can suppose that the two contours are close each other.
It is very interesting to compare the annotations on SLO images against the annotations on fundus images, both inter- and intra-annotator. In Table 6.6 are reported the results of this comparisons, with the three measurements.
On the diagonal we have the intra-annotator agreement on the two kind of images. We can see that often an annotator has a greater agreement with the fundus annotations of another doctor than with his own annotations. This result agrees also with the fact that the doctors found a difference in the difficulty of annotating the two kind of images.

[2]We don't have repeated annotation on fundus image for the annotator A1.

Table 6.6: Comparisons between annotators on the two kind of images.

Dice coefficient

		FUNDUS			
		A1	A2	A3	A4
SLO	A1	0.88 (0.06)	0.91 (0.06)	0.91 (0.06)	0.90 (0.08)
	A2	0.83 (0.08)	0.88 (0.07)	0.91 (0.06)	0.89 (0.08)
	A3	0.83 (0.07)	0.89 (0.05)	0.92 (0.05)	0.90 (0.08)
	A4	0.86 (0.07)	0.90 (0.05)	0.92 (0.05)	0.90 (0.08)

Jaccard coefficient

		FUNDUS			
		A1	A2	A3	A4
SLO	A1	0.78 (0.09)	0.83 (0.08)	0.84 (0.09)	0.82 (0.12)
	A2	0.71 (0.10)	0.80 (0.10)	0.84 (0.10)	0.81 (0.12)
	A3	0.71 (0.10)	0.80 (0.08)	0.86 (0.07)	0.82 (0.11)
	A4	0.76 (0.10)	0.83 (0.08)	0.86 (0.08)	0.83 (0.11)

Contour distance

		FUNDUS			
		A1	A2	A3	A4
SLO	A1	29 (16.85)	23 (15.44)	21 (16.82)	25 (21.34)
	A2	36 (18.64)	25 (15.96)	21 (16.35)	25 (21.94)
	A3	35 (15.64)	25 (9.74)	18 (9.32)	23 (19.56)
	A4	31 (17.12)	23 (14.29)	19 (14.24)	23 (21.08)

We suggested to annotate some parts of the contour in which the annotators were in doubt. As we can infer from Table 6.7 and 6.8, the annotators A1, A2 ,A3 were in doubt on a large number of images in both the two type of images, while A4 were in doubt in 50% of the images in both SLO and fundus. The mean (and std.dev.) is calculated over all the 50 images; for each annotator, in the images in which only one contour was traced, meaning no doubts on the boundary of the OD, we considered the second choice contour equal to the first choice contour (Dice, Jaccard = 1, contour distance = 0). This analysis between the two contours gives us an idea of how uncertain the determination of the contour is.

Table 6.7: Red Vs Yellow in SLO images

	# images	*Dice* *mean (std. dev.)*	*Jaccard* *mean (std. dev.)*	*Contour distance* *mean (std. dev.)*
A1	42	0.93 (0.07)	0.87 (0.10)	20 (15.83)
A2	41	0.95 (0.06)	0.90 (0.09)	15 (15.95)
A3	41	0.92 (0.06)	0.86 (0.10)	19 (11.55)
A4	25	0.97 (0.05)	0.95 (0.08)	9 (15.59)

Table 6.8: Red Vs Yellow in Fundus images

	# images	*Dice* *mean (std. dev.)*	*Jaccard* *mean (std. dev.)*	*Contour distance* *mean (std. dev.)*
A1	39	0.96 (0.04)	0.93 (0.07)	15 (14.87)
A2	43	0.96 (0.04)	0.93 (0.06)	13 (11.16)
A3	49	0.88 (0.05)	0.79 (0.09)	29 (10.67)
A4	25	0.97 (0.04)	0.95 (0.07)	8 (9.91)

6.3.1 PPA identification

Paripapillary atrophy (PPA) is the loss condition of retinal pigment epithelium and choriocapillaris located on the retina. The presence of PPA is associated with two kinds of diseases, namely glaucoma and myopia. Glaucoma and myopia are diseases that may cause blindness. Glaucoma is the second largest cause of blindness in the world and it is an incurable disease. Myopia is a disease widely suffered by both children and adults.
PPA is an area that has a distinctive texture, visually tends to be white. It lies adjacent to the outer boundary of optic disc and is described as a bright rounded area. Visually, the shape of PPA can be illustrated as a crescent moon, while in several cases the shape looks like ring because it appears around the OD.
PPA has so far been differentiated into zones: *alpha zone, beta zone and gamma zone*. It has been shown that the beta zone was associated with the presence of glaucoma, whereas the gamma zone was associated with the absence of glaucoma [39].
We asked to the annotators to place dots along the contour of the PPA, if present. From the analysis of the PPA segmentation results some interesting observations:

- The probability that the annotators agree, defined as the number of images in which they agree divided by the total number of images is 0.63 in SLO images, and 0.62 in FUNDUS ones.

- The percentage of images in which the i-th annotator ($i = 1, \ldots, 3$) identifies the PPA and at least one other annotator marks it as a contour: SLO = 0.56 mean (0.29 std.dev.), FUNDUS = 0.52 mean (0.40 std.dev.). To a better understanding look at Figure 6.8, 3th and 4th columns. This is a very interesting results because it implies an high variability in the PPA identification inter-annotators.

- We tested also the annotators agreement, so defined:

    - Number of images in which the annotators agree on the presence of PPA divided by the total number of images, SLO = 0.45, FUNDUS = 0.57.

- Number of images in which the annotators agree on the contour of PPA divided by the total number of images, SLO = 0.45, FUNDUS = 0.46, Figure 6.8, 1th and 2th columns.
- Number of images in which the annotators agree on the contour of PPA divided by the number of images in which they agree on the presence, SLO = 0.83, FUNDUS = 0.17.
  We can state that when all the annotators find a PPA in an image, so they agree on the PPA presence, they agree more in drawing the contour in SLO images, than in fundus one.

- The last interesting observation is the comparison between SLO and fundus with the same annotators: number of images in which the contour of the PPA is the same in the two kind of images. The 'Presence' coloumns are the number of images in which the i-th annotators recognized a PPA.

		Presence	
	Intra-agreement	SLO	FUNDUS
A1	0.73	9	15
A2	0.59	28	16
A3	0.55	26	13

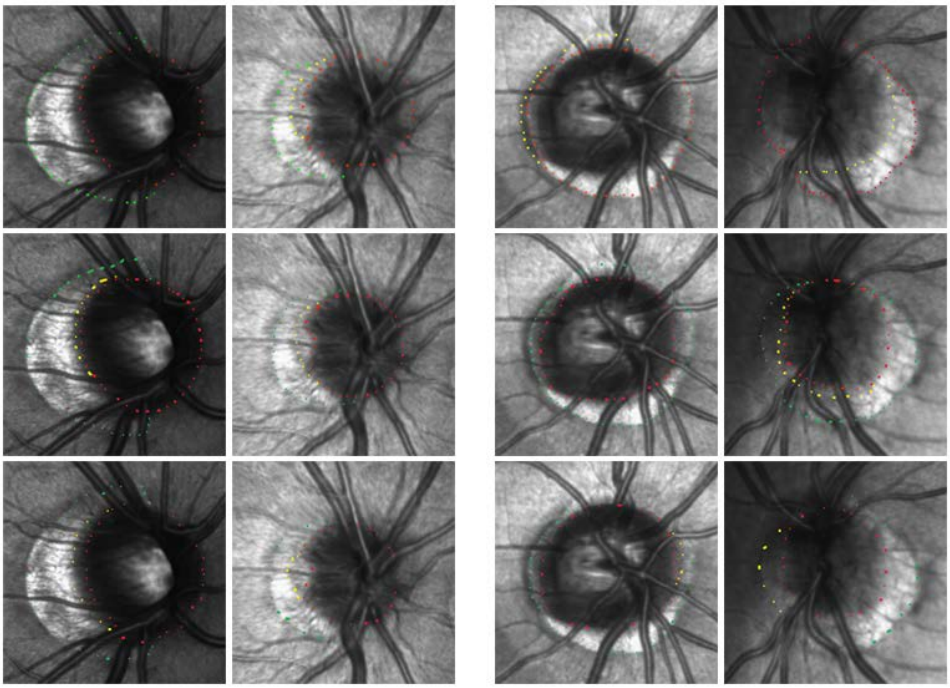

Figure 6.8: Form left to right, the first two columns show images in which the three annotators, one for each row, agree on the segmentation of the PPA (green dots). The other two columns show images in which when an annotator recognizes a zone as PPA at least another annotator marks the same zone as OD contour, first or second choice (red and yellow, respectively).

We made this analysis when we had only three annotators, so the above numbers are related to three annotators. Furthermore, we don't use any quantitative measurements to evaluate the segmentation, just visual inspection. From this study it appears that there is an high variability between annotators in drawing the PPA contour, as well as high variability intra-operator in drawing the contour in the two kind of images. Moreover it seems to be more easier for the three annotators to recognize the PPA in SLO images than in fundus ones, suggesting more studies on this topic.

6.4 Quantitative comparisons

In this Section we will evaluate the performance of the proposed methods and of VAMPIRE algorithm, as well as the comparison between the methods. The test are conducted as described in the 'Test planning' Section 2.4.
For simplicity, we refer to the methods as:

- '*Elliptical OD rim approximation via morphological operations*' **M1**
- '*Hand-crafted features for OD contour points selection*' **M2**
- '*VAMPIRE algorithm*' **V**

We compared the results obtained from the first method both with the ellipse (M1E) and the free-form segmentation (M1S) against human annotations on SLO images, Table 6.9.

Table 6.9: Performance of M1E and M1S compared to SLO ground truth.

	Dice *mean (std. dev.)*	*Jaccard* *mean (std. dev.)*	*Contour distance* *mean (std. dev.)*
M1E/A1	0.87 (0.08)	0.78 (0.11)	32 (19.96)
M1E/A2	0.90 (0.07)	0.83 (0.10)	25 (18.89)
M1E/A3	0.90 (0.07)	0.82 (0.11)	25 (19.16)
M1E/A4	0.88 (0.08)	0.79 (0.12)	30 (22.02)
M1S/A1	0.82 (0.09	0.71 (0.12)	40 (20.30)
M1S/A2	0.87 (0.07)	0.77 (0.10)	31 (16.36)
M1S/A3	0.89 (0.08)	0.80 (0.11)	27 (17.49)
M1S/A4	0.87 (0.09)	0.78 (0.12)	32 (22.22)

From the Table 6.9 we can see that by constraining the automatic segmentation to an elliptical shape, in M1, an improvement in performance is achieved, especially in the distance of the contours. Furthermore, also from visual inspection the results obtained with the ellipse looks more similar to the annotations. For these reasons we decide to take as algorithm's output the ellipse.
In Table 6.10 we reported the comparisons of the algorithm M2 with annotated SLO images. While in Table 6.11 the results of M2 are compared with the annotated fundus images, after being registered.

Table 6.10: Performance of M2 compared to SLO ground truth.

	Dice *mean (std. dev.)*	*Jaccard* *mean (std. dev.)*	*Contour distance* *mean (std. dev.)*
M2/A1	0.91 (0.06)	0.83 (0.10)	23 (14.74)
M2/A2	0.89 (0.06)	0.81 (0.10)	24 (13.31)
M2/A3	0.89 (0.08)	0.81 (0.11)	26 (20.87)
M2/A4	0.91 (0.05)	0.83 (0.08)	22 (13.31)

Table 6.11: Performance of M2 compared to fundus ground truth.

	Dice *mean (std. dev.)*	*Jaccard* *mean (std. dev.)*	*Contour distance* *mean (std. dev.)*
M2/A1	0.87 (0.08)	0.78 (0.10)	32 (19.48)
M2/A2	0.90 (0.07)	0.83 (0.10)	25 (19.29)
M2/A3	0.90 (0.07)	0.82 (0.10)	25 (18.93)
M2/A4	0.88 (0.08)	0.80 (0.11)	29 (21.60)

By looking at Table 6.12 we can see that in average the second method performs better than the first one. The advantage of having a free-form contour instead of an ellipse reflects in a better values in the 'contour distance' coloumn. Moreover the computational time is strongly inferior for M2 than M1. The time required for segmenting one image for M1 is $\sim$ 18.3 seconds while for M2 $\sim$ 2.6 seconds. In addition the first method rely only on morphological operations trying to segment the OD as connected component. For this reason we may suppose that in case of lesions the algorithm will fail. This is just a guess since our dataset is quite simple.
For all these reasons we can state that the second proposed method is best than the first one both in terms of accuracy and computational performance. Moreover, the method M2 performs well compared to the reference standards. In Figure 6.9 is shown the frequencies of images of M2 and annotators (in average) for decreasing value of the Dice coefficient. We can see that the manual procedure have a fairly large coefficient and there are few outliers for the automatic method making the average coefficient lower.

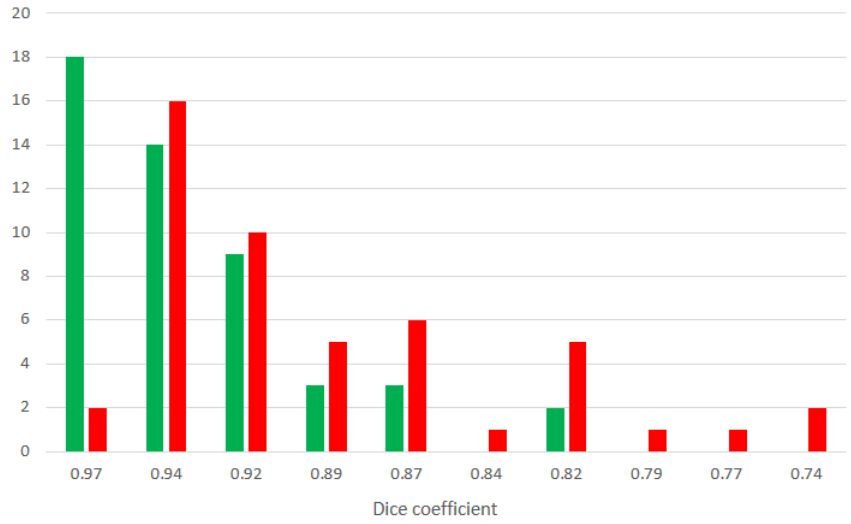

Figure 6.9: Histograms showing the number of automatic contours M2 (red) and SLO ground truth (green).

We can observe that the M2 performance compared to SLO GT and fundus GT gives results slightly different, contextually to the differences found in the inter-operators variability in the two kind of images (Table 6.6). We may suppose that the two kind of images give different informations about the optic disc contour.
In all our comparisons the Dice and Jaccard coefficients agree with slightly lower value of the last one. In the same way the values of the point-to-point distance agree with the other two indices.

We tested also the performance of the validate algorithm V against the annotated fundus of our dataset; the results are shown in Figure 6.10. In orange the performances of V against fundus annotated images and in blue M2 against SLO annoted images. The agreement between our method and annotators is comparable to the agreement between VAMPIRE algorithm and annotations on fundus images. This suggests us that we can consider our method as a valid proposal for OD segmentation in SLO images.

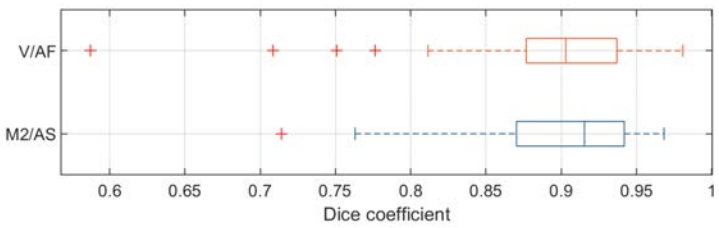

Figure 6.10: Orange box represents the performance of VAMPIRE algorithm on fundus images compared with annotations of fundus images. Blue box represents the performance of M2 algorithm on SLO images compared with annotations of SLO images. The line inside the box is the median value and the red '+' symbols are the outliers.

The 'Summary Table' 6.12 shows the average measurements of the methods against reference standard, as well as inter and intra-annotators.

Table 6.12: Summary table: average coefficients (and standard deviation) for the automatic procedures compared with intraoperator and interoperator coefficients.

	Dice *mean (std. dev.)*	*Jaccard* *mean (std. dev.)*	*Contour distance* *mean (std. dev.)*
Average M1 vs A_SLO	0.89 (0.07)	0.80 (0.11)	28 (20.13)
Average M2 vs A_SLO	0.90 (0.07)	0.82 (0.10)	24 (16.61)
Average V vs A_fundus	0.89 (0.08)	0.82 (0.08)	28 (20.81)
Average inter-op. SLO	0.93 (0.06)	0.88 (0.09)	15 (12.98)
Average intra-op. SLO	0.96 (0.03)	0.92 (0.05)	10 (6.87)
Average M2 vs A_fundus	0.89 (0.07)	0.81 (0.11)	28 (19.94)
Average inter-op. fundus	0.92 (0.06)	0.88 (0.09)	20 (14.96)
Average intra-op. fundus	0.96 (0.02)	0.93 (0.04)	9.88 (5.96)

6.5 Chapter summary

In this Chapter we described tests conducted in a pilot validation of our methods for OD segmentation. The results show a good agreement of our automatic methods with the annotators, comparable with the validated algorithm.
For what concerning the annotations is evident the uncertain in the OD contour. Inter-annotation variability indicates an interesting level of disagreement on the exact location of the OD contour, especially in the fact that all the annotators were in doubt in a lot of images tracing a double contour choice. Moreover, particular attention must be paid to the segmentation of the PPA, which was very variable within the annotators.

Chapter 7

Conclusions and future works

The aim of this thesis is to develop an algorithm for automatic locating and segmenting the optic disc (OD) in scanning laser ohptalmoscope images (SLO). From the interfacing with doctors a great variability emerged in the definition of the contour of the optic disc and so the need of an automatic procedure for the segmentation.
We proposed two original methods inspired by the relevant literature for this purpose. The '*Elliptical OD rim approximation via morphological operations*' locates the OD relying on the fact that the OD in this kind of images appears as the largest connected component. Through a sequence of morphological operations it segments the OD approximating with an elliptical shape.
The '*Hand-crafted features for OD contour points selection*' shares the locating procedure with the first method and then computes *ad hoc* features around the OD. The final contour is identified by an optimization in the space of the possible shapes of a deformable contour.
The second method performs better than the first one compared to the gold standards and it is faster in terms of computational time. This method is being incorporated in the VAMPIRE software for OD location in Heidelberg Spectralis SLO images, under development by the VAMPIRE Edinburgh group.
In addition, we presented a semi-automatic routine to register the SLO and fundus images. In this way we were able to compare the information on the OD resulting from the two retinal imaging techniques, as well as the results of a validate algorithm for fundus images and our method.
To sum up our main findings, for simplicity only in terms of Dice coefficients, refer to Figure 7.1. The inter-annotator agreement is high except in some images and overall is higher between SLO annotated images than in the fundus ones. The SLO OD segmentation results show excellent agreement with the SLO ground truth (M2/AS), suggesting the algorithm's suitability for pratical applications, comparable with the agreement of the OD detection in fundus camera images (V/AF). Interestingly, both agreements are similar to inter-observer ones for both fundus and SLO images. It is worth noticing the lower mean agreement between the method and fundus ground truth (M2/AF) respect to SLO GT (M2/AS), comparable with the lower annotators agreement between the two kind of images (AS/AF) respect to the inter-agreement in

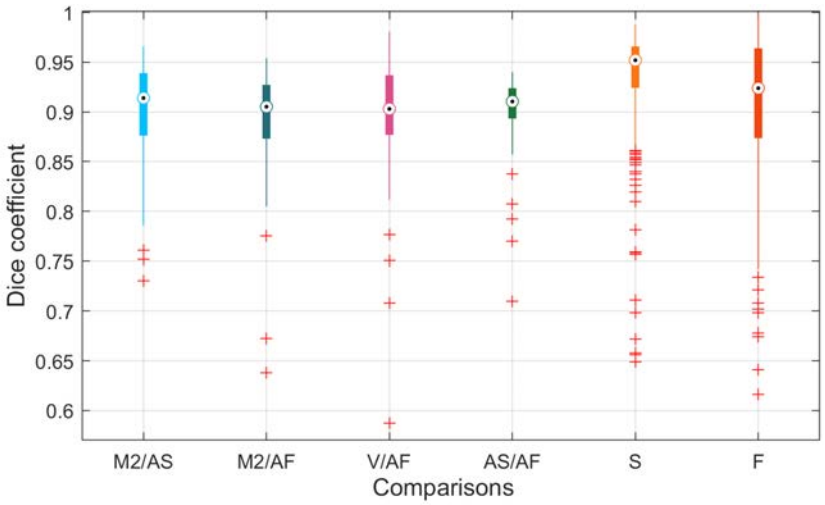

Figure 7.1: In the box plot the comparison between: our method (M2), VAMPIRE (V), annotations on SLO (AS), and annotations on fundus images (AF). In orange, the annotators agreement on SLO (S) and fundus images (F). On each box, the central mark indicates the median, and the bottom and top edges of the box indicate the 25th and 75th percentiles, respectively. The whiskers extend to the most extreme data points not considered outliers, and the outliers are plotted individually using the '+' symbol.

SLO (S) and in fundus (F).

A limitation to our results is the fact that we had a local dataset and it is free of lesions. In future it could be useful assessing the performance of our methods on larger public datasets with some lesions, as well as comparing with methods designed for SLO images.
Everything in our work, methods and tests, has been implemented in MATLAB. A first improvement to our method could be provide with an optimization phase. Furthermore our algorithm works with images of dimension 1536x1536; it could be modified in future such that it can works with different image resolutions.
Another idea is to return with the OD segmentation also measurements of the four characteristics of the optic nerve head: optic nerve tilt, crescent, ovality and torsion. In fact, it has been demonstrated that changing in these characteristics are associated with the progression of pathologies as myopia and glaucoma [40].
Another improvement to our method is to return as algorithm outcome the PPA segmentation in addition to the OD segmentation. As discussed in Section 6.3.1, we found a large variability in the segmentation of the PPA within the annotators. Moreover we observed discrepancies in locating and segmenting the PPA in SLO and fundus images of the same retina, both intra-annotators and inter-annotator. In our dataset the annotators show a greater agreement in SLO images, than in fundus ones, suggesting that the SLO images are suitable to study this pathology. These considerations suggest to both develop

automatic procedure to segment the PPA zones and to investigate the PPA appearance in the two images to understand if one kind of image is better than the other in identifying the PPA.
Regarding the approach used to registered the images we can state that our registration method suffers from a manual step that makes the procedure time consuming and tedious. It could be useful in a future work to make the first part of the procedure, control points selection, automatic.
A last hint for a possible study is investigate the differences in the OD contour resulting from the annotations in the SLO and fundus images. Since the annotations are different, it could be possible to understand if the two types of retinal imaging give us different information about the OD and it could be understood which kind of images is the best for studying the optic disc.

Appendix

Optic disc annotation protocol in SLO Heidelberg Spectralis images

Sabrina Mattera, Stefano Gennari, Tom MacGillivray and Emanuele Trucco
s.mattera, s.gennari, e.trucco@dundee.ac.uk
VAMPIRE project
Version: 8th April 2019

1. Purpose and context
The purpose of this exercise is to generate a set of ground truth (gold standard) optic disc contours in matched pairs of Heidelberg Spectralis SLO images and fundus camera images.

The context is the development of a VAMPIRE application capable of computing morphometric properties of the vasculature in Heidelberg Spectralis SLO image, complementing the existing VAMPIRE applications for fundus camera images and ultra-wide-field-of-view OPTOS SLO images. The contours ("annotations"), will be used to validate a VAMPIRE software application detecting the OD contour automatically.

For each retina, a fundus camera image is also provided.

2. Methods
For simplicity, we recommend to use Microsoft Paint. Our guidelines refer to Microsoft Paint for Windows 10, version 1803. If Microsoft Paint is not available on your operative system, please contact us before starting the annotations.
We suggest to annotate two contours per OD: one showing the most likely contour in your opinion, and a second, where needed, showing a plausible alternative for possible, uncertain parts of the contour.
In case of visible *peripapillary atrophy* (PPA) in the image, we ask you to annotate it with a third contour.

A contour is annotated by placing (clicking) points along it. For guidance, e.g. frequency of points, a few examples of annotated contours are provided.
Please check these before starting your annotations.

Feel free to zoom in to place your contour points if this helps you.

3. Loading the images
Download the archive <*Heildelberg SPECTRALIS.zip*> and extract all the files.

4. Annotation protocol

4.1 Look at the examples

Start by looking at the examples of annotated contours in the directory <*Protocol and annotation examples*>. This will show you what your annotations should look like. The different colours are explained below. If you have questions, please contact Sabrina, Stefano and Manuel (emails above) before starting.

4.2 Annotate the images

Please try to annotate the whole set of images consistently, e.g. in similar conditions, and dedicating comparable amounts of time and attention to each image.

The SLO images to be annotated and corresponding fundus camera images are located in the directory <*Images to annotate*>.
The SLO images are in the format '.tif', while fundus images are in the format '.bmp'.
Please, it is required to annotate the SLO and fundus images independently.

To annotate a new image:

1. Open the image in Paint.
2. Place red dots along your first choice of contour. To do this, select 'brush' and 'size' as shown in Figure 1. For number/frequency, please follow the examples.
3. If you are uncertain about some parts of the contour, place yellow dots along your second choice of contour.
4. If PPA is visible, place green dots along the contour.
5. Save the annotated image as <*name*>*ann.tif* ; for instance, the annotated version of image
05.tif would be *05ann.tif*.

It would be useful if you could record on a separate file the time taken per image.

5. Images for repeatability

Please, once you have completed the annotations, we ask you to produce a second annotation for a batch of 30 images (15 SLO, 15 fundus) randomly chosen. We will use this set of annotations in order to compute the repeatability.

Please re-annotate without looking the first annotation.

6. Returning the annotated images

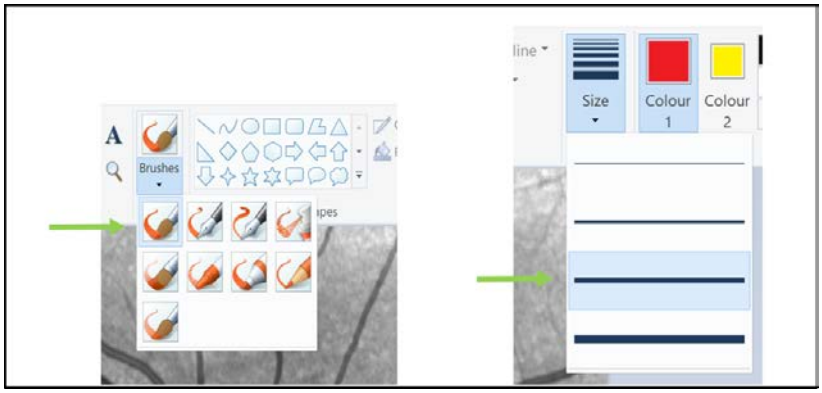

Figure 1. Paint menus. Left: please select the brush indicated by the arrow in the Brushes menu. Right: please select the thickness indicated by the arrow in the Size menu. Colour (red for first-choice contour, yellow for second-choice one) can be selected using the adjacent boxes.

Please upload the annotated images in the Dropbox directory and alert Sabrina and Stefano.

Thank you very much for your collaboration and time.

Bibliography

[1] Lee Ann Remington, Chapter 4 - Retina, Editor(s): Lee Ann Remington, Clinical Anatomy and Physiology of the Visual System (Third Edition), Butterworth-Heinemann, 2012, Pages 61-92.

[2] MacGillivray, Tom & Trucco, Emanuele & Cameron, James & Dhillon, Baljean & Houston, John & Beek, Edwin. (2014). Retinal Imaging as a Source of Biomarkers for Diagnosis, Characterisation and Prognosis of Chronic Illness or Long-Term Conditions.. The British journal of radiology. 87. 20130832. 10.1259/bjr.20130832.

[3] https://www.nhs.uk/conditions/diabetic-retinopathy/

[4] MacGillivray T., McGrory S., Pearson T., Cameron J. (2018) Retinal Imaging in Early Alzheimer's Disease. In: Perneczky R. (eds) Biomarkers for Preclinical Alzheimer's Disease. Neuromethods, vol 137. Humana Press, New York, NY.

[5] Facey K, Cummins E, Macpherson K, Morris A, Reay L, Slattery J. 2002. Organisation of services for diabetic retinopathy screening. Health technology assessment report 1. Glasgow: Health Technology Board for Scotland.

[6] Gramatikov, Boris. (2014). Modern technologies for retinal scanning and imaging: An introduction for the biomedical engineer. Biomedical engineering online. 13. 52. 10.1186/1475-925X-13-52.

[7] Patton, Niall & Aslam, Tariq & Macgillivray, Thomas & J Deary, Ian & Dhillon, Baljean & Eikelboom, Robert & Kanagasingam, Yogesan & Constable, Ian. (2006). Retinal image analysis: Concepts, applications and potential. Progress in retinal and eye research. 25. 99-127. 10.1016/j.preteyeres.2005.07.001.

[8] Shankaranarayana S.M., Ram K., Mitra K., Sivaprakasam M. (2017) Joint Optic Disc and Cup Segmentation Using Fully Convolutional and Adversarial Networks. In: Cardoso M. et al. (eds) Fetal, Infant and Ophthalmic Medical Image Analysis. OMIA 2017, FIFI 2017. Lecture Notes in Computer Science, vol 10554. Springer, Cham.

[9] Noronha, Kevin & Nayak, K. (2012). Fundus image analysis for the detection of diabetic eye diseases-a review. 2012 International Conference on Biomedical Engineering, ICoBE 2012. 10.1109/ICoBE.2012.6179013.

[10] Reis, Alexandre & P Sharpe, Glen & Yang, Hongli & Nicolela, Marcelo & Burgoyne, Claude & Chauhan, Balwantray. (2012). Optic Disc Margin Anatomy in Patients with Glaucoma and Normal Controls with Spec-

tral Domain Optical Coherence Tomography. Ophthalmology. 119. 738-47. 10.1016/j.ophtha.2011.09.054.

[11] E. Trucco, A. Ruggeri, T. Karnowski, L. Giancardo, E. Chaum, J. P. Hubschman, B. al-Diri, C. Y. Cheung, D. Wong, M. Abràmoff, et al. "Validating Retinal Fundus Image Analysis Algorithms: Issues and a Proposal". In: Investigative Ophthalmology & Visual Science 54.5 (2013), pp. 3546–3559.

[12] Jadhav, Rahul & Narnaware, Manish. (2017). Review on Segmentation Techniques used in Optic Disc and Blood Vessel Segmentation. International Journal of Emerging Research in Management and Technology. 6. 115-120. 10.23956/ijermt/SV6N4/113.

[13] Balaji, G.N. & V. Suryanarayana, S & Babu Kakarla, Naresh. (2018). Computer Aided Optical Disc Detection in Fundus Images: A Review. CVR Journal of Science & Technology. 14. 58-63. 10.32377/cvrjst1412.

[14] Thakur, Niharika & Juneja, Mamta. (2018). Survey on segmentation and classification approaches of optic cup and optic disc for diagnosis of glaucoma. Biomedical Signal Processing and Control. 42. 162-189. 10.1016/j.bspc.2018.01.014.

[15] Sinthanayothin,C, Boyce, J. F. , Cook, H. L. and Williams, T.H. "Automated localisation of the optic disc, fovea and retinal blood vessels from digital colour fundus images", British J. of Ophthalmology, Vol. 83, No.8, pp. 902–910, Aug 1999.

[16] Muhammad, Abdullah & Fraz, Muhammad & A. Barman, Sarah. (2016). Localization and segmentation of optic disc in retinal images using Circular Hough transform and Grow Cut algorithm. PeerJ. 4. e2003. 10.7717/peerj.2003.

[17] Giraddi, Shantala & Pujari, Jagadeesh & Hiremath, Prakash. (2017). Optic disc detection using geometric properties and GVF snake. 141-146. 10.1109/ICISIM.2017.8122164.

[18] Hoover, Adam & Goldbaum, Michael. (2003). Locating the optic nerve in a retinal image using the fuzzy convergence of the blood vessels. IEEE transactions on medical imaging. 22. 951-8. 10.1109/TMI.2003.815900.

[19] Ruggeri, Alfredo & Forrachia, M & Grisan, Enrico. (2003). Detecting the optic disc in retinal images by means of a geometrical model of vessel network. 1. 902 - 905 Vol.1. 10.1109/IEMBS.2003.1279911.

[20] X. Wu, B. Dai and W. Bu, "Optic Disc Localization Using Directional Models," in IEEE Transactions on Image Processing, vol. 25, no. 9, pp. 4433-4442, Sept. 2016. doi: 10.1109/TIP.2016.2590838.

[21] Perez-Rovira, Adria & Trucco, Emanuele. (2010). Contextual optic disc location in retinal fundus images. Journal of Modern Optics - J MOD OPTIC. 57. 136-144. 10.1080/09500340903434526.

[22] Osareh, Alireza & Mirmehdi, Majid & T. Thomas, Barry & Markham, Richard. (2002). Comparison of Colour Spaces for Optic Disc Localisation in Retinal Images. 1. 743-746. 10.1109/ICPR.2002.1044865.

[23] Chuang Wang, Djibril Kaba, and Yongmin Li, "Level Set Segmentation of Optic Discs from Retinal Images," Journal of Medical and Bioengineering, Vol. 4, No. 3, pp. 213-220, June 2015. Doi: 10.12720/jomb.4.3.213-220.

[24] Huiqi Li and O. Chutatape, "Automated feature extraction in color retinal images by a model based approach," in IEEE Transactions on Biomedical Engineering, vol. 51, no. 2, pp. 246-254, Feb. 2004. doi: 10.1109/TBME.2003.820400.

[25] Dehghani, Amin & Moghaddam, Hamid & Moin, Mohammad-Shahram. (2012). Optic disc localization in retinal images using histogram matching. EURASIP Journal o/n Image and Video Processing. 2012. 10.1186/1687-5281-2012-19.

[26] A. Giachetti, L. Ballerini, and E. Trucco, "Accurate and reliable segmentation of the optic disc in digital fundus images," Journal of Medical Imaging 1, 024001 (2014).

[27] S. Gennari, "An investigation into deep learning for locating the optic disc in scanning laser ophthalmoscope retinal images", 2019 (Thesis).

[28] Lagarias, Jeffrey & A. Reeds, James & H. Wright, Margaret & Wright, Paul. (1998). Convergence Properties of the Nelder–Mead Simplex Method in Low Dimensions. SIAM Journal on Optimization. 9. 112-147. 10.1137/1052623496303470.

[29] Fitzgibbon, Andrew & Pilu, Maurizio & Fisher, Robert. (2000). Direct Least Square Fitting of Ellipses. IEEE Transactions on Pattern Analysis and Machine Intelligence. 21. 10.1109/34.765658.

[30] Rafael C. Gonzales and Paul Wintz. 1987. Digital Image Processing (2nd Ed.). Addison-Wesley Longman Publishing Co., Inc., Boston, MA, USA.

[31] Nicolao, Giuseppe & Sparacino, Giovanni & Cobelli, Claudio. (1997). Nonparametric Input Estimation in Physiological Systems: Problems, Methods, and Case Studies. Automatica. 33. 851-870. 10.1016/S0005-1098(96)00254-3.

[32] Goshtasby, Ardeshir, "Piecewise linear mapping functions for image registration," Pattern Recognition, Vol. 19, 1986, pp. 459-466.

[33] Goshtasby, Ardeshir, "Image registration by local approximation methods," Image and Vision Computing, Vol. 6, 1988, pp. 255-261.

[34] Bashiri, Fereshteh S. & Baghaie, Ahmadreza & Rostami, Reihaneh & Yu, Zeyun & D'Souza, Roshan. (2018). Multi-Modal Medical Image Registration with Full or Partial Data: A Manifold Learning Approach. Journal of Imaging. 5. 5. 10.3390/jimaging5010005.

[35] Reel, Parminder Singh; S. Dooley, Laurence; Wong, K.C.P; Börner, Anko (2014): Multimodal retinal image registration using a fast principal component analysis hybrid-based similarity measure. figshare. Poster.

[36] Mani, V.R.s & Selvaraj, Arivazhagan. (2013). Survey of medical image registration. Journal of Biomedical Engineering and Technology. 1. 8-25.

[37] C. Heneghan, P. Maguire, N. Ryan and P. de Chazal, "Retinal image registration using control points," Proceedings IEEE International Symposium on Biomedical Imaging, Washington, DC, USA, 2002, pp. 349-352. doi: 10.1109/ISBI.2002.1029265.

[38] Heneghan, Conor & Maguire, Paul. (2003). Registration of opthalmic images using control points. Proceedings of SPIE - The International Society for Optical Engineering. 10.1117/12.463688.

[39] Dai, Yi & B Jonas, Jost & Huang, Haili & Wang, Min & Sun, Xinghuai. (2013). Microstructure of Parapapillary Atrophy: Beta Zone and Gamma Zone. Investigative ophthalmology & visual science. 54. 10.1167/iovs.12-11255.

[40] Marsh-Tootle, Wendy & Harb, Elise & Hou, Wei & Zhang, Qinghua & A. Anderson, Heather & Weise, Katherine & T. Norton, Thomas & Gwiazda, Jane & Hyman, Leslie. (2017). Optic Nerve Tilt, Crescent, Ovality, and Torsion in a Multi-Ethnic Cohort of Young Adults With and Without Myopia. Investigative Opthalmology & Visual Science. 58. 3158. 10.1167/iovs.16-20860.